Mechanisms of heat transport across the Southern Greenland continental shelf in two eddy-active ocean/sea-ice simulations

Theresa J. Morrison[1], Dmitry S. Dukhovskoy[2], Julie L. McClean[1], Sarah T. Gille[1], Eric P. Chassignet[2]

[1]Scripps Institution of Oceanography, University of California San Diego, La Jolla, CA
[2]Center for Ocean-Atmospheric Prediction Studies, Florida State University, Tallahassee, FL

Key Points:

- Cross-shelf heat transport is strongest over the southeast continental shelf in both ocean models
- Shelf currents bring heat to the southwest shelf, where winds drive off-shelf heat transport
- Topographic Rossby waves generated near the Denmark Strait impact cross-isobath heat transport

Corresponding author: Theresa J. Morrison , `T4Morris@ucsd.edu`

Abstract

The increased presence of warm Atlantic water on the Greenland continental shelf has been connected to the accelerated melting of the Greenland Ice Sheet, particularly in the southwest and southeast shelf regions. Results from two eddy-permitting coupled ocean-sea ice simulations are used to understand the transport of heat on and off the southern Greenland shelf. The analysis reveals that the region of greatest heat transport onto the shelf is southeast Greenland. On the southwestern shelf, heat is mainly exported from the shelf to the interior basins. Full heat budgets for a series of control volumes on the Greenland shelf are analyzed to identify the mechanisms that drive cross-shelf heat transport. Two mechanisms of shelf-basin heat exchange are explored: wind-driven exchange and topographic Rossby waves generated near the Denmark Strait. The heat and volume transports do not depend directly on the winds, and differences in wind forcing between the two simulations may contribute only slightly to differences in properties on the shelf and in the transport of heat across the shelf. Topographic Rossby waves are observed in both simulations along the southeast shelf break; in both models they modify cross-shelf transport as they propagate clockwise along the shelf. On the southern shelf, warm water is spread to the southeast and then southwest Greenland by coastal and boundary currents.

Plain Language Summary

Melting of the Greenland Ice Sheet has been accelerating in recent decades because of rising ocean and air temperatures. Warm ocean water in the deep basin from the subtropical North Atlantic is separated from the ice sheet margin (glacier termini in the Greenland fjords) by the shallower continental shelf region. In this study we compare two simulations of the ocean and sea ice that represent the currents and eddying motions around Greenland realistically. We identify how and where heat is moved on and off the southern Greenland shelf and consider the results to be robust when they are common to both simulations. We find that warm water mainly moves onto the southeast shelf and off the southwest shelf; the currents on the shelf transport the warm water around the southern tip of Greenland. Winds do not directly move heat on or off the shelf. Near the Denmark strait we identify oscillations, known as topographic Rossby waves, that propagate southwards along the shelf producing intrusions of warm water onto the shelf during their

passage. Understanding how warm water reaches the shelf allows us to better understand how the ocean contributes to the melting of the Greenland Ice Sheet.

1 Introduction

Mass loss from both the Greenland and Antarctic Ice Sheets remains the major source of uncertainty in projecting global sea level rise (Meehl et al., 2007). The Greenland Ice Sheet (GIS) is losing mass at an increasing rate, from 51 $\pm$ 17 Gt/y in the 1980s to 286 $\pm$ 20 Gt/y in the 2010s (Mouginot et al., 2019). Since 1972, this mass loss has contributed to 13.7 $\pm$ 1.1 mm of global sea level rise (Mouginot et al., 2019). Recently B. Smith et al. (2020) reported a total mass loss of 200 ± 12GT/y from 2003 to 2019. Projections of sea level rise due to ice sheet mass loss emphasize the short-term (next 100 years) importance of the GIS as oceanic and atmospheric temperatures rise (Meehl et al., 2007). The lack of representation of both ice sheet dynamics and connections to the ocean and atmosphere in climate models contributes significantly to the uncertainty of those projections. An estimated $15-25\%$ of total mass loss from the GIS is from melting tidewater glaciers with an additional $15-25\%$ from calving fluxes (Benn et al., 2017); both processes increase as the ocean warms.

The margin of the GIS is comprised of both land terminating and marine terminating glaciers; the tidewater terminating glaciers are the primary connection between the ocean and the GIS through deep narrow fjords. Warm salty water of Subtropical North Atlantic origin is thought to provide the source of heat needed for ocean-driven melting (Straneo & Heimbach, 2013; Rignot et al., 2012); the co-location of Atlantic-originated water and tidewater glaciers makes the southeastern portion of the GIS particularly vulnerable to ocean-driven melting (Millan et al., 2018). Over the southeast portion of the GIS, the observed mass loss (Luthcke et al., 2006; van den Broeke et al., 2009; Wouters et al., 2008) is, in part, attributed to warming ocean conditions (Howat et al., 2008), but it is difficult to separate these effects from those of atmospheric warming (Straneo et al., 2013; Hanna et al., 2013). The presence of warm water on the southwest shelf has also been observed (Sutherland et al., 2013; Straneo et al., 2012). Observations from specific glacial fjords have shown warming of ocean water preceding glacial retreat events (Christoffersen et al., 2012; Holland et al., 2008), implying that in some regions heat from the ocean may be the leading driver of ice sheet mass loss. Within fjords, observations have provided estimates of the penetration of warm water to the front of glaciers (Jackson et al., 2014) given the presence of Atlantic water on the shelf.

Comprehensive observations of the subpolar and polar oceans are uniquely challenging to obtain (G. C. Smith et al., 2019). Therefore, the available data are often sparse and irregularly sampled. Ocean models can be used to better understand the ocean circulation in these regions, as they provide a complete temporal and spatial record. However, the production of realistic simulations in these regions is challenging. There are limited observations (Morlighem et al., 2017; An et al., 2019) of the topography of the Greenland shelf, particularly the fjord bathymetries. In atmospherically forced simulations of the ocean, the quality of the atmospheric forcing will determine the accuracy of the ocean's response. In addition, simulations that aim to study shelf and near-shelf processes require high resolution in those regions, making them computationally expensive.

The Greenland continental shelf is impacted by the fresh and cold water masses exported from the Arctic Ocean as well as the warm and salty water masses advected from the North Atlantic (Figure 1) (after Holliday et al., 2018). Warm water from the subtropical gyre is advected into the subpolar gyre by the North Atlantic Current (NAC), an extension of the Gulf Stream. The NAC consists of multiple northward branches; eastward branches enter the Nordic seas, while those to the west retroflect to enter the Irminger Current (Holliday et al., 2018). Just south of the Denmark Strait, the Irminger Current retroflects, and its primary branch heads southward along the Greenland continental shelf break. On the Greenland Shelf, from the Fram Strait to Cape Farewell, the East Greenland Current (EGC) flows southward, advecting cold fresh water from the Arctic and seasonal sea ice melt. At Kangerdlugssuaq Trough, the smaller East Greenland Coastal Current (EGCC) develops (Sutherland & Pickart, 2008) onshore of the EGC. The circulation along the East Greenland Shelf is characterized by cold fresh shelf waters and by warmer saltier waters off the shelf in the Irminger Basin. Warm water in the basin cannot easily cross onto the shelf because the shelf break is a barrier to onshore transport. In an unforced system, a water parcel will conserve potential vorticity by balancing the Coriolis force f and the height of the water column h. To cross the shelf break, changing h by moving from a deep basin to a shallow shelf, a source of potential energy is needed.

Figure 1. Schematic of circulation in the Subpolar North Atlantic. Major currents are labeled: North Atlantic Current (NAC), East Reykjavik Ridge Current (ERRC), Irminger Current (IC), East Greenland Current (EGC), East Greenland Coastal Current (EGCC), West Greenland Current (WGC), Labrador Current (LC), Baffin Current (BC), North Icelandic Jet (NIJ), Iceland-Faroe Current (IFC), Faroe-Shetland Current (FSC), Norwegian Atlantic Current (NwAC), and West Spitsbergen Current (WSC). The major transects used to divide the on-shelf regions are labeled 1-6: (1) Davis Strait, (2) Cape Farewell Gate, (3) Sermilik Gate, (4) Denmark Strait, (5) Fram Strait, and (6) Nares Strait. (after Holliday et al., 2018) with additions from (Sutherland & Pickart, 2008; Håvik et al., 2017; Saini et al., 2020; Furevik & Nilsen, 2005; Rossby et al., 2018).

In this paper, we aim to understand the processes that could drive cross-isobath exchange at the Greenland Continental Shelf, and we therefore look into previous studies of analogous shelves. For example, the Antarctic Continental Shelf is a similar high-latitude shelf which, in some regions, has cold water on the shelf, strong shelf currents, and warm water in the deep basin in a configuration that is analogous to southeast Greenland. Studies of mechanisms of heat transport onto the Antarctic Continental Shelf have been similarly motivated by the need to better understand ocean-driven melting of the Antarctic Ice Sheet. These studies have explored possible drivers for the on-shelf transport of warm Circumpolar Deep Water across the Antarctic continental shelf break. Winds along the Antarctic Slope position the pycnocline at the shelf break to balance the eddy-driven on-shelf transport of Circumpolar Deep Water (Stewart & Thompson, 2015). Weakened easterly winds shoal isotherms, while freshening on the shelf opposes the shoaling, re-enforcing the importance of both winds and lateral density gradients in cross-shelf transport (Goddard et al., 2017). In regions where the Antarctic Slope Front is strong (from the Weddell Sea to the Ross Sea, including East Antarctica) eddy stirring along the front has been found to be a key mechanism for heat transfer (Stewart et al., 2018). Palóczy, Gille, and McClean (2018) found using the same high-resolution POP simulation used in this study, see Section 2.1 for details, that the mean heat transport onto the Antarctic Continental Shelf is controlled by Ekman convergence over the shelf. Coastal troughs play a key role in the pathways of Circumpolar Deep Water onto the continental shelf; Dinniman, Klinck, and Smith Jr (2011) found that warm water intrusions in a trough in the West Antarctic Peninsula were linked to short-duration wind events. The mechanisms found to transport Circumpolar Deep Water across the Antarctic Slope are likely to be relevant to the Greenland Continental Shelf and provide the motivation for the mechanisms we will explore to explain cross-shelf heat transport around Greenland.

For the Greenland Shelf, thus far there have not been studies akin to the Antarctic investigations of mechanisms governing on-shelf heat transport and the resulting warming. A recent study from Gillard, Hu, Myers, Ribergaard, and Lee (2020) focused on troughs around the shelf with a focus on heat reaching fjords. Other model based studies have found high-frequency variability along the southeast Greenland Continental Shelf occurs in high-resolution regional simulations (Moritz et al., 2019; Gelderloos et al., 2021) and cyclonic eddies formed at the Denmark Strait propagate along the shelf break (Moritz et al., 2019). Coastal trapped waves in this region have been identified in a high-resolution simulation from subinertial variability (Gelderloos et al., 2021) though the waves were not specifically defined as topographic Rossby waves.

Questions then arise as to how efficiently heat is transported onto the shelf, and in what regions. Understanding which processes drive the transport of warm Atlantic water onto the shelf will help better project what changes to the regional winds, local stratification, or circulation on the shelf could be linked to increased vulnerability of tidewater glaciers to ocean-driven melting. Therefore, our study focuses on understanding both the mechanisms governing the resulting pattern of temperature variability on the shelf using two coupled ocean–sea-ice simulations performed with the Parallel Ocean Program (POP) and the HYbrid Coordinate Ocean Model (HYCOM), respectively. By comparing temperature on the shelf and the cross-shelf heat transport in the two simulations, we are able to gain insight into the dominant mechanisms of shelf–basin exchange. The two simulations are configured differently and use different atmospheric forcing and therefore are independent experiments in which the mechanisms that drive on-shelf heat transport and shelf–basin exchange are explored.

In Section 2, we begin with a description of the models and, in Section 3, compare model results to observations. Next, in Section 4, we calculate cross-isobath volume and heat transports and then examine the spatial patterns of temperature and cross-shelf heat transport in southern Greenland. We look at the heat flux through key gates around the shelf to gain insights into the heat flux of the East Greenland Current system on the continental shelf, with the understanding that our models resolve limited dynamics on the shelf. We find seasonal and daily variability, motivating the exploration of two mechanisms. In Section 5, a primary cross-isobath exchange mechanism is proposed for each timescale: wind-driven exchange on the seasonal scale and topographically trapped waves that modify cross-shelf exchange on a multi-day timescale. Finally, we discuss the robust dynamics identified by comparing these two independent simulations.

2 Model Description

We compare two coupled ocean sea-ice models with horizontal resolutions comparable to the first baroclinic Rossby radius of deformation in this region (4–8 km in the deep ocean). Models with this resolution are classified as "eddy-permitting" (Dukhovskoy et al., 2016; Nurser & Bacon, 2014). The effective grid spacing in POP is $\sim$5–6 km and

$\sim$4-5 km in HYCOM. The first baroclinic Rossby radius is smaller on the continental shelf (2-4 km Nurser & Bacon, 2014); both models have limited ability to capture smaller mesoscale processes on the shelf, in the next section a description of what shelf mesoscale processes are that captured is presented. Each model is forced by a different set of atmospheric observations, but neither assimilates data. This allows each model to act as an independent representation of the dynamics in this region. Both models are coupled to the same sea-ice model and do not include any representation of freshwater from GIS melt. Each simulation is described in further detail in the next subsections.

2.1 POP 0.1° - CICE 4

In this study, we use results from a global 62-year (1948-2009) simulation of the Parallel Ocean Program version 2 (POP2; Dukowicz & Smith, 1994) and the Community Ice Code version 4 (CICE4; E. C. Hunke et al., 2010) coupled together in the Community Earth System Model (CESM; Hurrell et al., 2013) version 1.2 framework (McClean et al., 2018). The ocean and sea-ice components are coupled every 6 hours using Flux Coupler 7 (CPL7, Craig et al., 2012). For further details on this simulation, see (Wang et al., 2018; Palóczy et al., 2018, 2020; Castillo-Trujillo et al., 2021; Arzeno-Soltero et al., 2021). This simulation is referred to as POP from here on in the text.

The ocean and sea-ice models are on a 0.1° tripolar grid with nominal horizontal resolution of $\sim$5–6 km in our study region. POP has 42 non-uniformly spaced vertical levels; they range from 10-m spacing at the surface to 250 m in the deep ocean. At 800 m depth, the vertical spacing is approximately 200 m. The bathmyetry is based on ETOPO2 with minor modifications in the Arctic (more details are given by McClean et al. (2011)). Partial bottom cells are used to more smoothly represent the bathymetry. The ocean model has an implicit free surface and is globally volume conserving.

Sub-gridscale horizontal mixing of momentum and tracers in POP is represented using bi-harmonic operators. The horizontal viscosity and diffusivity coefficients depend on the horizontal grid spacing, with equatorial values of -2.7×10^{10} m^4 s^{-1} and -0.3×10^{10} m^4 s^{-1}, respectively, varying with the cube of the average grid cell length. The K-profile parameterization (Large et al., 1994) is used to represent vertical mixing. This simulation setup does not include any explicit tidal forcing or additional mixing from tidal dissipation.

POP's ocean properties, potential temperature and salinity, were initialized from the World Hydrographic Program Special Analysis Center climatology (Gouretski & Koltermann, 2004). A 17-day stand-alone (without CICE4) spin-up integration was run using very short time steps to allow high-amplitude transients to equilibrate. The coupled ocean/sea ice simulation was then initialized from the end state of the 17-day POP simulation. The atmospheric forcing is given by the Coordinated Ocean-ice Reference Experiment–II (CORE-II) corrected interannually varying fluxes (CIAF; Large & Yeager, 2009)) and has a horizontal resolution of $\sim 1.9^\circ$. Starting in 1980, climatological values of radiation and precipitation are replaced with time-varying data based on observations. Ocean surface evaporation and precipitation fluxes and runoff are implemented using virtual salt fluxes; a surface salinity restoring condition with an effective timescale of about 4 years limits model drift.

Sea-ice velocities are defined by the dynamic component of CICE4 based on the elastic-viscous-plastic (EVP) rheology of E. Hunke and Dukowicz (1997). Sea-ice and snow growth rates are defined by the thermodynamic component of CICE4 based on the energy conserving sea ice of Bitz and Lipscomb (1999). The Delta-Eddington multiple scattering parameterization is used to represent solar radiation transfer between ice and snow (Briegleb & Light, 2007).

The sea-ice state was initialized from a uniform 2-m thick layer with the ice edge defined by the January climatological ice edge from Special Sensor Microwave Imager (SSM/I) observations. In the POP simulation, the Arctic sea ice adjusted over a longer period than in the Antarctic, with potentially excessive melt and export through the Fram Strait during the 1960s. This long adjustment and excessive export could be a transient solution from the initialization of the simulation. Another alternative is that the climatological period of the atmospheric forcing (1948-1980) exaggerates a large-scale forcing that could increase sea-ice export.

We use output from the last five years of the simulation for our analysis. For this period, daily averages of the model variables were saved.

2.2 0.08° Arctic Ocean HYCOM - CICE 4

The second model used in this study results from numerical experiments by Dukhovskoy et al. (2019) conducted using regional 0.08° Arctic Ocean HYbrid Coordinate Ocean Model

(HYCOM) (Bleck, 2002; Chassignet et al., 2003, 2007) coupled to CICE4. This simulation is referred to as HYCOM in the text.

The model domain is a subset of the global HYCOM (Chassignet et al., 2009; Metzger et al., 2014) north of 38°N. The computational grid of the 0.08° HYCOM-CICE is a Mercator projection from the southern boundary to 47°N. North of 47°N, it employs an orthogonal curvilinear Arctic dipole grid (Murray, 1996). The model has effective spacing of ~4-5 km in the Subpolar North Atlantic. The model topography is derived from the Naval Research Laboratory Digital Bathymetry Data Base 2-minute resolution (NRL DBDB2). In the current configuration, HYCOM employs a vertical grid with 41 hybrid layers that provide higher resolution in the upper 1500 m. This simulation is one-way nested within the 0.08° Global HYCOM +Navy Coupled Ocean Data Assimilation (NCODA) 3.0 reanalysis (Metzger et al., 2014) (for 1993–2005) and Global Ocean Forecasting System (GOFS) 3.1 analysis (for 2006–2016).

Atmospheric forcing fields are obtained from the National Centers for Environmental Prediction (NCEP) Climate Forecast System Reanalysis (CFSR) (Saha et al., 2010) for 1993–2011 and CFSv2 (Saha et al., 2014) for 2012–2016. More details on the model configuration and computational grid as well as model validation and analysis of the model experiments are given by Dukhovskoy et al. (2019, 2021).

3 Model Validation

3.1 Continental Shelf Control Volumes

To understand how warm Atlantic water crosses onto the shelf and where it is present, the shelf and shelf break must be clearly defined. Shallow straits and deep troughs make choosing a single isobath for the shelf break challenging. However, we found the 800 m isobath to be representative of the shelf break; our results were not sensitive to small changes in the choice of isobath. The contour surrounds Greenland, starting and ending at the Nares Strait connecting to Ellesmere Island (see Figure 2). The exact depths of the shelf break in each model (see Figure 2) show how the bathymetry of the two simulations differs. See supplemental material for a detailed map of the Southeast region highlighting the troughs and small scale bathymetry.

In addition to the shelf break, we define six control volumes to examine spatial differences in cross-isobath transports and properties on the shelf. The boundaries are spec-

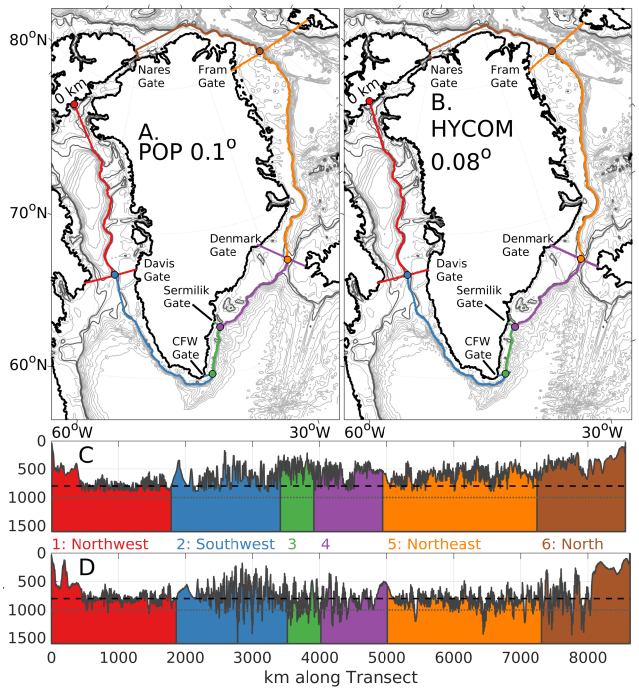

Figure 2. Map of circum-Greenland transects in (A) POP and (B) HYCOM, subdivided at the major straits and gates and plotted over the regions' bathymetries. The 800 m isobath is followed in both models, with the exact depth along the transect plotted for (C) POP and (D) HYCOM with the regions numbered; the black dashed line is 800m and the gray dashed line is 1000m. Shelf regions are: (1) Northwest, (2) Southwest, (3) Narrow Shelf, (4) Wide Shelf, (5) Northeast, and (6) North. Together Sections 3 and 4 constitute the Southeast region. The color of the contour in each region corresponds to the bathymetry plotted for that region. A regional map of the Southeast region directly comparing the two bathymetries is provided in the supplemental materials.

ified at major straits or "gates" to differentiate heat transport regionally. The fluxes at the gates are also computed, providing a representation of the circulation on the shelf. However, neither model fully resolves the sub-mesoscale dynamics that are important for circulation on the shelf. These straits and gates (hereafter collectively referred to as gates when considering only the portion between the coast and 800 m isobath) are labeled in Figure 1. The contour begins at the west side of Ellesmere Island (0 km), and the along-transect distance used in this paper is measured from that point counterclockwise, first south along western Greenland then north along eastern Greenland. Therefore, along the contour, the gates are in order: (1) Davis Gate, (2) Cape Farewell Gate, (3) Sermilik Gate, (4) Denmark Gate, (5) Fram Gate, and (6) Nares Gate with the Nares Gate marking the eastern end of Nares strait and the end of the circum-Greenland contour. Between these gates we define the regional control volumes of the continental shelf as: (1) Northwest, (2) Southwest, (3) Narrow Shelf, (4) Wide Shelf, (5) Northeast, and (6) North, labeled in Figure 2. The Southeast region has been subdivided into the Narrow and Wide sections because of differences in the cross-shelf exchange that we observed along the shelf break.

3.2 Comparison to Observations

The variables most critical for calculating volume and heat transports are velocity and temperature. Since we are interested in eddy and mean processes, we consider both the strength of the mean currents and the spatial distribution and magnitude of the eddy kinetic energy (EKE). For temperature validation we focus on the temperatures in the Irminger Current as it is the major source of oceanic heat advected into our region of interest. We look at the sea ice distribution on the southeast shelf in both models. In addition, we compare the wind stress used to force each simulation.

The 2005-2009 climatology of speed averaged over the top 50 m of both models is shown in Figure 3. Both models show some evidence of the observed slope and coastal currents off southeast Greenland. The East Greenland Coastal Current has an offshore length scale of one Rossby radius but is present in both simulations, indicating that the resolution of the models is sufficient to capture some important mesoscale processes but not smaller-scale eddies. The currents strongly follow bathymetric contours, indicating the possibility that topographic steering plays a leading role in transport across the shelf break. North of Sermilik Trough (see Figure 1), between the coast and nearby troughs

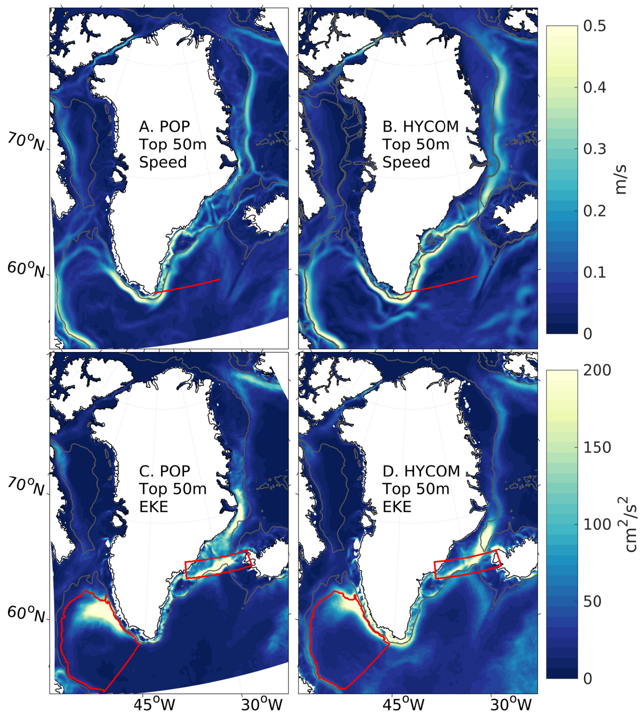

308 **Figure 3.** Average speed in the top 50 m over 2005-2009 for POP (A) and HYCOM (B).
309 Average Eddy Kinetic Energy over the same period in the top 50 m over 2005-2009 for POP (C)
310 and HYCOM (D). In (A,B) the red line shows the transect at 60°N. In (C,D) the boundary of
311 two control volumes are shown in red: the interior Labrador Sea defined by the 2,000 m isobath
312 and a box at the Denmark Strait.

there is a better defined coastal current in POP than in HYCOM. At 60°N, the Cape Farewell Gate marked by the red line in Figure 3, the peak velocity in HYCOM is 64 cm s^{-1} at a position 120 km from the coast. In POP there are two peaks in the surface speed: 35 cm s^{-1} located 97 km from the coast and 42 cm s^{-1} located 155 km from the coast. See supplemental material for more details. This difference in current structure contributes to the difference in net transport onto the shelf between the two models (Figure 4). In general, the currents follow narrower pathways in POP than in HYCOM, possibly indicating less meandering. This is also supported by the higher EKE along the shelf break in HYCOM.

We calculate the EKE from the daily averages of velocity. We define

$$\mathrm{EKE} = \frac{u'^2 + v'^2}{2} \tag{1}$$

with $u' = u - \overline{u}$, where u is the daily average velocity and $\overline{u}$ is the monthly average of velocity. This defines eddies as anomalies that have a period between two days and one month. To obtain the near-surface expression of EKE, we use only the velocity in the top 50 m. The 2005-2009 climatology is plotted in Figure 3. In both models, west of Greenland there is an expanse of elevated EKE extending into the central Labrador Sea (outlined in red in Figure 3 (C) and (D)). This represents an important pathway for the transport of heat and freshwater from the shelf into the Labrador Sea. The region of elevated EKE in POP starts at the shelf break, in contrast with HYCOM, which has elevated EKE on and off the shelf, possibly indicating a difference in the cross-shelf exchange between the two models in this region. EKE estimated from TOPEX/Poseidon satellite altimetry (Brandt et al., 2004) and surface drifters (Fratantoni, 2001) in this region shows a similar pattern of elevated EKE in the eastern Labrador Sea. The surface EKE from Brandt et al. (2004) in the West Greenland Current ranges from 400 to 800 cm^2 s^{-2} for the period 1997-2001. Altimeter-based estimates are generally higher than those calculated here, which are based on velocity in the top 50 m. Estimates from 15 m drogued satellite-tracked surface drifter paths from 1990-1999 are 400 to 500 cm^2 s^{-2}, which is consistent with the maximum EKE of both models within the defined interior Labrador Sea control volume (shown in red in Figure 3). In POP, the maximum EKE is 432 cm^2 s^{-2} while in HYCOM it is 527 cm^2 s^{-2}. The average EKE in HYCOM is 53.2 cm^2 s^{-2}, with the 20th to 80th percentiles ranging from 20.0 to 62.9 cm^2 s^{-2}. POP values are similar: mean EKE is 51.1 cm^2 s^{-2}, with 20th to 80th percentiles from 10.1 to 82.0 cm^2 s^{-2}. The EKE of

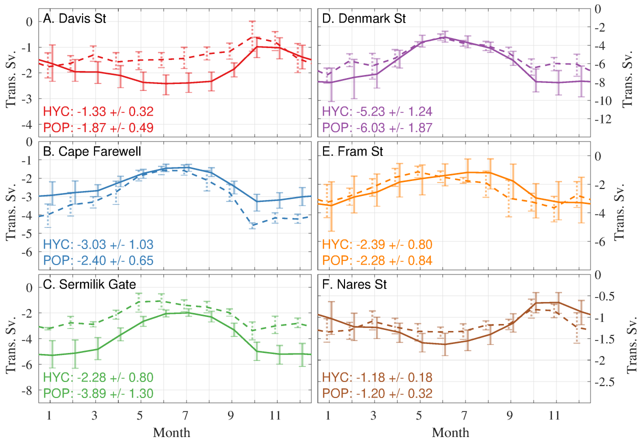

Figure 4. Volume fluxes through transects defined in Figure 2 from POP (solid lines) and HYCOM (dashed lines) and error bars at the 20th and 80th percentiles; the annual mean and standard deviation are included on each plot. Transports are from (A) Davis Strait (B) Cape Farewell Gate (C) Sermilik Gate (D) Denmark Strait (E) Fram Strait and (F) Nares Strait; here strait refers to the entire transect between two land masses and gate refers to transport between the Greenland coast and the defined shelf break. Negative transport is southward.

both simulations has a similar magnitude and location to those observed in the Labrador Sea.

A second region of elevated EKE is a large region spanning from the northeast shelf at Scoresby Sound to where the Irminger Current retroflects south of the Denmark Strait. This corresponds to a region of large sea surface height anomalies observed by AVISO (Trodahl & Isachsen, 2018). Heightened EKE near the Denmark Strait is also consistent with observations of mesoscale eddies and boluses formed at the Denmark Strait overflow (Moritz et al., 2019). The average EKE in the defined box just south of the Denmark Strait (outlined in red in Figure 3 (C) and (D)) is higher in POP (133 cm^2 s^{-2}) compared to HYCOM (80.7 cm^2 s^{-2}), and the maximum EKE in POP (958 cm^2 s^{-2}) is twice the maximum in HYCOM (429 cm^2 s^{-2}). In POP there is particularly strong band of EKE just south of the strait at the shelf break, while in HYCOM the maximum is broader and north of the strait.

To further compare the velocity of the two models, we look at the net volume transport though the defined gates. For gates associated with major straits (Davis Strait, Denmark Strait, Fram Strait, and Nares Strait), we compare the volume transport across the entire strait to observational-based estimates. We find both the magnitude and seasonal variability of volume transports to be consistent between the simulations. Figure 4 shows the mean seasonality for the transports in POP and HYCOM; negative values indicate southward volume transport. Observational-based estimates of transports through the same straits are shown in Table 1 with the 2005-2009 averages of both simulations. Uncertainties of observational-based estimates of oceanic fluxes in Fram Strait have been discussed (De Steur et al., 2018; Dushaw & Sagen, 2016) but apply broadly to straits in this region that are poorly sampled in space and time. In addition, transport through these straits varies interannually; the means presented may not be representative of the true mean.

The transport through the Fram Strait is the primary source of Arctic Water in the East Greenland Current. Both POP and HYCOM have estimates of the net volume transport through the Fram Strait that are consistent with observations that include the shelf currents. Volume transport through the Fram Strait has been shown to be sensitive to both the inclusion of moorings that measure the shelf currents as well as the latitude defining the strait (79°N vs 78.50°N). At the Denmark Strait, our model results are compared to an estimate of the overflow transport (defined as $\sigma_\theta > 27.8$ kg m^3), which is lower than our estimates of the total transport through the strait, as expected. At the Cape Farewell and Sermilik Gates, there are no constraining straits to use in defining transports; therefore, we focus on the continental shelf volume fluxes from the coast to the 800 m reference contour. At both gates there is similar magnitude and seasonality to the volume fluxes. The winter maximum at Sermilik gate is weaker in HYCOM compared to POP by roughly 1 Sv, but the summer minimum is similar in both models. Transport at the Cape Farewell Gate has the opposite difference; the winter maximum in HYCOM is 1 Sv greater than the maximum in POP. This is one indication that the cross-shelf exchange in the Narrow Shelf region is different in the two simulations. The Cape Farewell Gate is located at the same position as the Overturning in the Subpolar North Atlantic Program (OSNAP) mooring array at 60°N; for both models, the maximum transport is in winter, consistent with the observations of Le Bras, Straneo, Holte, and Holliday (2018). At the Davis Strait, the average volume transport in HYCOM is about 0.54 Sv less than in POP. Estimates of the volume transport from observations have a large range, but the estimate from Curry et al. (2014) that covers a similar time period to our study

Table 1. Comparison of Observed and Modeled Volume Transports Through Straits

Strait	Time Period	Volume Transport	Reference
Fram Strait	1997-2000	-4 ± 2 Sv	(Schauer et al., 2004)
Fram Strait	1997-2007	-2.0 ± 2.7 Sv	(Beszczynska-Moeller et al., 2011)
Fram Strait	2005	-1.6 ± 3.9 Sv	(Tsubouchi et al., 2012)
Fram Strait	2005-2010	-2.39 ± 0.80 Sv	HYCOM
Fram Strait	2005-2010	-2.28 ± 0.84 Sv	POP
Denmark Strait Overflow	2007–2011	3.4 ± 1.4 Sv	(Jochumsen et al., 2012)
Denmark Strait	2005-2010	-5.23 ± 1.24 Sv	HYCOM
Denmark Strait	2005-2010	-6.03 ± 1.87 Sv	POP
Davis Strait	1987-1990	-2.6 ± 1.0 Sv	(Cuny et al., 2005)
Davis Strait	2004-2005	-2.3 ± 0.7 Sv	(Curry et al., 2011)
Davis Strait	2004-2010	-1.6 ± 0.5 Sv	(Curry et al., 2014)
Davis Strait	2005-2010	-1.33 ± 0.32 Sv	HYCOM
Davis Strait	2005-2010	-1.87 ± 0.49 Sv	POP
Nares Strait	Summer 2003	-0.8 ± 0.3 Sv	(Münchow et al., 2006)
Nares Strait	2003-2006	-0.57 ± 0.09 Sv	(Münchow & Melling, 2008)
Nares Strait	2005-2010	-1.18 ± 0.18 Sv	HYCOM
Nares Strait	2005-2010	-1.20 ± 0.32 Sv	POP

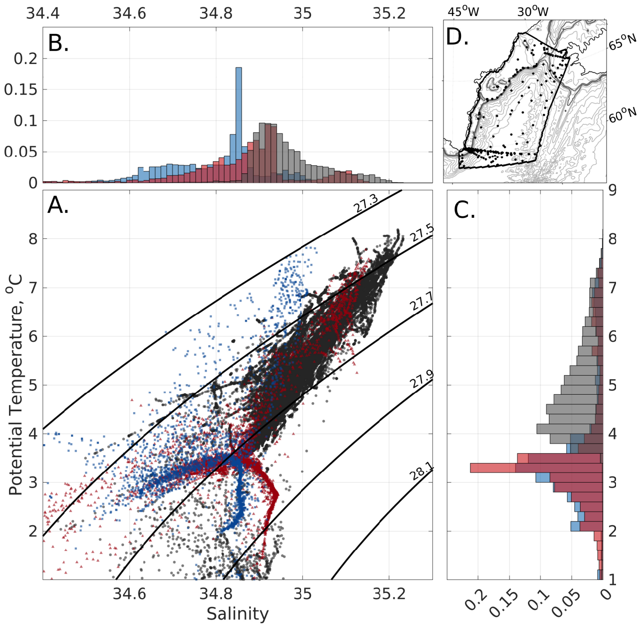

Figure 5. Comparison of WOA observations (gray), HYCOM (red), and POP (blue). (A) T-S diagram of observations from WOA (gray), HYCOM (red), and POP (blue). (B) Histogram of salinities from WOA, HYCOM, and POP, (C) same as (B) but for temperature. Locations of the WOA data are shown in (D) and limited to 200-800m depth.

has an average volume transport that falls within the range of both the POP and HYCOM simulations.

To validate the temperature and salinity properties of the models, we compared them to World Ocean Atlas (WOA) data collected in the eastern Irminger Sea. A control volume (map in Figure 5(D)) was chosen to include part of the Irminger Sea and the southeast continental shelf. Observations collected between 2005-2009 were used (see supplemental material for details). The monthly mean that coincided with the timing of a given observation was used in order to limit the impact of eddy variability, and the model was sub-sampled at the closest grid point to the observation. We analyzed depths from 200 m to 800 m to limit the impact of surface variability. Both simulated and observed data sets were binned in temperature–salinity (Θ-S) space to calculate probability density functions (Figure 5). Overall, this comparison shows that the models are colder and fresher than the observations. The mean temperature is 3.6$\pm$1.4°C in POP, 3.5$\pm$1.4°C in HYCOM, and 4.6$\pm$1.2°C in WOA, where ranges given here are one standard devi-

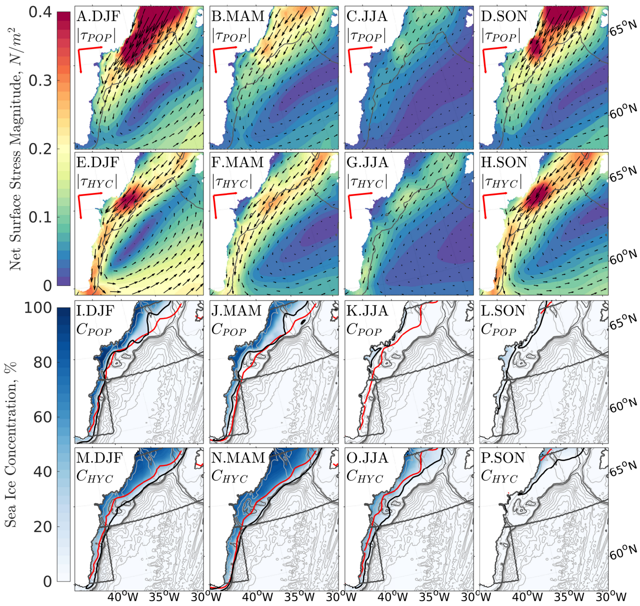

Figure 6. Seasonal averages of daily net surface stress fields from CORE-II CIAF from 2005-2009 used to force the 0.1° simulation (A-D) and CFSR forcing from 2005-2009 used for the HYCOM 0.08° simulation (E-H). Seasonal averages of sea ice concentration from 0.1°POP (I-L) and 0.08° HYCOM (M-P). The ice edge defined by the 15% concentrations from the model simulations are shown in black, and from SSM/I in red (25 km resolution).

ation. Similarly, POP is the freshest of the three data sets with a mean salinity of 34.8±0.13 PSU, compared to 34.8±0.20 PSU in HYCOM, and 35.0±0.08 PSU in WOA.

Over the East Greenland Continental Shelf, persistent northerly winds are downwelling favorable and play a significant role in setting up the currents on the shelf (Sutherland & Pickart, 2008). Where present, sea ice mediates how wind stress drives the ocean. Sea ice reflects more solar radiation than the ocean and limits the radiative transfer into the ocean, limiting the surface heat flux reaching the ocean surface. The northerly winds are strongest in the winter when sea ice extent is largest; the seasonal magnitude of the net surface stress driving each model is shown in Figure 6.

The sea-ice edge position is determined in part by the meandering and strength of the currents on the shelf. In Figure 3, the topographic steering at Kangerdlugssuaq Trough is more pronounced in POP. Similarly the sea-ice edge somewhat follows the topography of the trough. This difference in the two simulations is also pronounced at the Sermilik Troughs region, where the sea ice is usually shoreward of the troughs in POP but in HYCOM covers the entire shelf. We compare the total ice area in two boxes (black boxes in Figure 6), one covering the Narrow Shelf region and the other the Wide Shelf region. The total area covered by sea-ice in winter (December, January and February) in the SSM/I data is 0.6x10^6 km^2 in the Narrow Shelf box and 5.5x10^6 km^2 in the Wide Shelf box. In HYCOM and POP the winter sea-ice area in the Wide Shelf box is 5.9x10^6 km^2 and 3.8x10^6 km^2; in the Narrow Shelf box it is 1.0x10^6 km^2 and 0.7x10^6 km^2, respectively. Sea-ice area over the Wide Shelf box is consistently overestimated in HYCOM and underestimated in POP, with the exception of fall (September, October, and November) when POP has 60% more sea-ice area than SSM/I. In the Narrow Shelf box there is a less clear difference in the simulations and observations, both simulations have more fall and winter sea-ice by area that SSM/I. In the spring (March, April, and May) both models underestimate sea-ice area (47% in POP, 20% in HYCOM). For POP this continues into summer (June, July and August, 88% less than SSM/I), while in HYCOM it reverses (43% more than SSM/I).

The net surface stress includes both the wind stress and the stress from the sea ice onto the ocean. Over the shelf, the location and spatial structure of the strongest surface stress differ between the forcings. In the POP surface forcing, the maximum stress is over the Wide Shelf with two local maxima: one to the south of Kangerdlugssuaq Trough and the other to the north of Denmark Strait. In winter, these maxima are strongest and merge into a single region of high surface stress over the majority of the Wide Shelf region. The POP surface stress in the Narrow Shelf region is weaker than the stress over the Wide Shelf. The HYCOM surface forcing has a maximum south of Kangerdlugssuaq Trough that is similar in magnitude to the maximum in POP. However, the maximum to the north of the Denmark Strait is weaker and further offshore than the northern maximum in POP. The HYCOM surface stress along the Narrow Shelf and near Cape Farewell is higher and more coastally trapped than the surface stress in POP. There are moderate winds all along the southeast shelf slope throughout the year that are strongest at Cape Farewell.

The differences in sea-ice cover and sea-ice–ocean stress are not sufficient to explain the difference in the net surface stress between the two simulations in this region. We attribute the majority of the difference to discrepancies in the CORE2-IAF and CFSR wind products. These differences in wind stress would also drive sea-ice dynamics differently, thus compounding the difference in net surface stress. Overall, the surface stress is stronger in POP over the Wide Shelf region; in HYCOM the region of high net surface stress is weaker but extends father south to Cape Farewell. These differences could be a primary driver of differences in cross-shelf transports and the shelf currents.

Overall, our models compare well with each other and with observations. The resolution allows for shelf break currents with realistic strength and seasonality. The transports through major straits are consistent among the two models and observations. The water masses present in both models and observations are similar with moderate temperature biases in both models. The wind stresses used to force each simulation have significant differences in spatial structure over the southeast Greenland Shelf but similar seasonal cycles.

3.3 Heat Transport Definition

Volume fluxes are calculated using daily means of velocity. The net volume transport across the 800 m isobath is defined as

$$V_{800} = \int_H^0 \int_0^L \hat{v}\, d\hat{x}\, dz, \tag{2}$$

where $\hat{x}$ is the along-boundary direction and $\hat{v}$ is the velocity component perpendicular to the transect. In the case of the 800 m isobath, the normal direction, n, is defined such that $\hat{v} = v\dot{n}$ is onto the shelf. In the case of the gates, the volume flux is calculated similarly, but the normal direction is northward. This allows us both to look at the overall volume flux onto the shelf and to construct budgets for the individual shelf regions by considering whether the gate is at the northern or southern boundary of the region. (If the gate is the northern boundary, the normal direction must be reversed to point into the box.) Both models are volume conserving, with small free surface variations. Therefore we can use volume budgets to validate our transport estimates.

Heat flux is calculated using daily means of potential temperature and velocity from both models. For the heat transport across the 800 m isobath we define

$$\Phi_{800} = \int_H^0 \int_0^L \rho c_p(\theta - \theta_{ref})\hat{v}\, d\hat{x}\, dz, \tag{3}$$

where ρ is the density of seawater, c_p is the specific heat capacity of seawater, and θ is the reference potential temperature. This definition is used both for the transport across the 800 m isobath (Φ_{800}), and through the various gates (Φ_G). As with the volume transport, positive volume flux is onto the shelf, and gate fluxes are positive in the northern and eastern directions.

Changes in the heat content of a specified volume are given by the heat fluxes integrated over the bounding surface. Here, the change in heat of a given volume is defined by the convergence of the lateral ocean fluxes, the net surface heat flux, and heat storage (change in heat content of the control volume):

$$\rho c_p \frac{d\Theta_{vol}}{dt} = (\Phi_{800} + \Phi_{G-north} + \Phi_{G-south}) + \Phi_{SHF}. \tag{4}$$

Without having saved the heat storage term as the model ran, we cannot close the heat budget exactly. Using daily averages we can approximate the change in heat content over time, but acknowledge that there is some variability that is obscured by the daily averaging. Surface heat fluxes from the HYCOM simulations were not saved. The choice of reference temperature does not change the net heat transport into an enclosed region (Bacon & Fofonoff, 1996; Schauer & Beszczynska-Möller, 2009). We have used a reference temperature $\theta_{ref} = -1.8°$C, which is the salinity-independent freezing temperature in POP (R. Smith & Gent, 2002).

4 Results

4.1 Heat Content of the Southeast Shelf

Many tidewater glaciers terminate in the Southeast region, making the region important to ocean-driven melting of the GIS (Millan et al., 2018). We specifically examine the vertical structure of the average temperature, shown in Figure 7 in four layers: surface (0-50 m), mid-depth (50-200 m), shelf bottom (200-800 m), and deep (800 m to bottom). On the shelf, the importance of bathymetry in controlling warming is apparent as warm water is present in areas with deeper bathymetry. The two main regions of warm water on the shelf at all depths are in the Kangerdlugssuaq and Sermilik Troughs.

The HYCOM shelf water is colder than that in POP, with average temperatures in the Wide Shelf region of 0.95±0.55°C versus 2.15±0.64°C, respectively (see Table 2 for average temperatures in each control volume). The position of the warm–cold front in the upper layers is primarily along the 800 m isobath in HYCOM (E and F) but is further onshore in POP (A and B). Warm water incursions onto the shelf over deep bathymetry, such as Kangerdlugssuaq Trough and Sermilik Deep, in the surface layer are stronger in

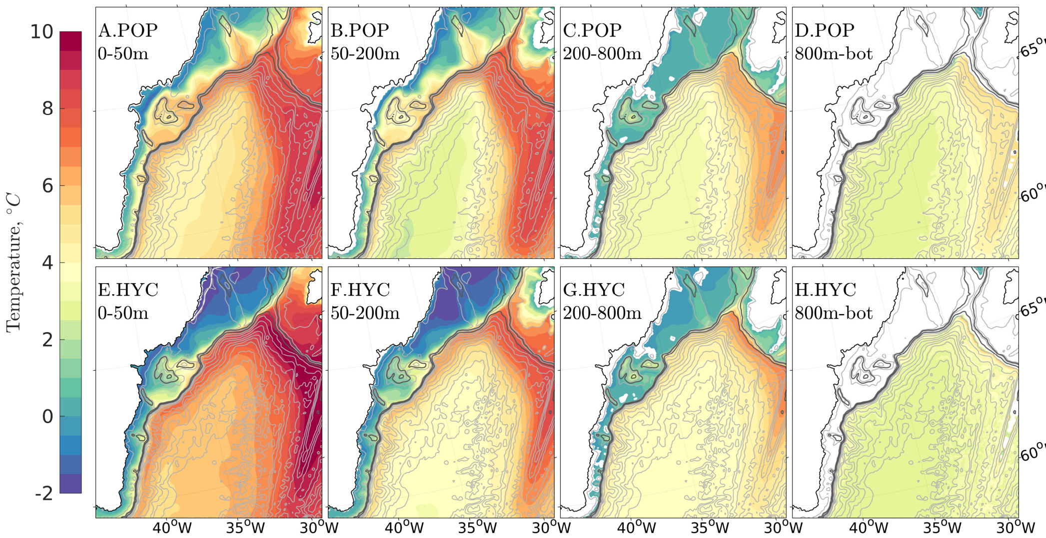

Figure 7. Climatology from 2005-2009 of potential temperature in POP (A-D) and HYCOM (E-H) for depth ranges: 0-50 m (A,E), 50-200 m (B,F), 200-800 m (C,G), and 800 m–bottom (D,H). Bathymetry contours are shown in light gray, with the 500 m and 800 m isobaths in dark gray.

POP (A and B) compared to HYCOM (E and F). This is consistent with the topographically steered current speed observed in the top 50 m (Figure 3); note the difference in bathymetry at the mouth of the trough (supplemental material). This difference is reduced in the 200-800 m layer, (C for POP, G for HYCOM) as are differences in the Irminger Basin temperature. The water within the Irminger Basin is generally warmer in HYCOM than in POP; here the basin is defined as the region deeper than the 800 m isobath and north of 60°N, the region enclosed by the black contour in Figure 7. The average basin temperature in the surface layer of HYCOM (E) is 6.9°C; the average in POP (A) is 6.1°C. This difference between the two models is not present from 50 - 800 m, where the basin temperatures differ by <0.1°C, but from 800 m to the bottom, POP (D) is 0.5°C warmer than HYCOM (H).

4.2 Average Transports onto the Greenland Shelf

Figure 8 shows the 5-year climatology of the vertically integrated volume (A for POP and D for HYCOM) and heat (B for POP and E for HYCOM) fluxes in each simulation in 100 km sections of the contour. The gates are marked along the plot to show which regions have the strongest fluxes and warmest temperature. The average temper-

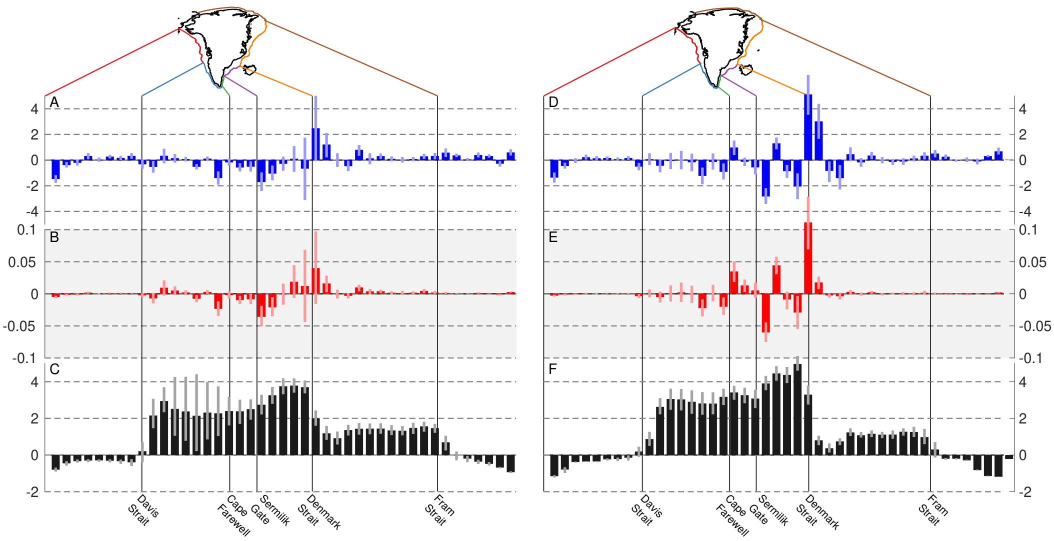

Figure 8. Bar graph of net volume fluxes (Sv, blue), net heat fluxes (PW, red), and average temperature (°C, black) in 100 km sections of the transect for POP (A-C) and HYCOM (D-F). For both volume and heat fluxes, positive values indicate flux onto the shelf. Dark bars are the 5 year average from 2005-2009, with light bars representing the 20th and 80th percentile range. In both models, the strongest on shelf fluxes are near the Denmark Strait. In POP this maximum is associated with strong variability; in HYCOM the heat flux is consistently onto the shelf at this location.

Table 2. Average Transports Through Gates and Across the Shelf.

Section	Length (km) POP	Length (km) HYCOM	V (Sv) POP	V (Sv) HYCOM	Φ (TW) POP	Φ (TW) HYCOM	T_avg (°C) POP	T_avg (°C) HYCOM
Northwest Shelf	1,785	1,864	-1.34±0.51	-1.46±0.44	-6.11±5.86	-5.54±4.76	-0.27±0.18	-0.65±0.15
Davis Gate	166	192	0.25±0.74	-0.27±0.59	8.52±13.2	-7.85±9.73	-	-
Southwest Shelf	1,622	1,651	-2.40±0.79	-2.15±0.84	-29.9±10.4	-16.6±16.0	1.96±1.36	1.96±0.84
Cape Farewell Gate	77	62	-2.62±0.75	-2.45±0.85	-38.7±19.8	-33.4±18.6	-	-
Narrow Shelf	503	503	-1.13±0.62	-0.59±0.45	-18.0±13.9	28.2±15.7	1.65±1.02	1.41±0.81
Sermilik Gate	74	87	-3.53±1.20	-3.03±1.12	-53.2±21.6	-39.5±21.9	-	-
Wide Shelf	1,021	994	-0.90±0.66	0.77±0.76	16.4±13.8	55.0±23.3	2.15±0.64	0.95±0.55
Denmark Gate	257	361	-4.07±1.42	-2.28±0.95	-33.2±18.9	-13.0±8.43	-	-
Northeast Shelf	2,315	2,303	3.07±1.11	1.63±0.90	44.2±19.6	16.1±8.17	0.11±0.37	-0.62±0.17
Fram Gate	298	266	-0.99±0.48	-0.62±0.23	-1.84±1.57	-0.94±0.60	-	-
North Shelf	1,314	1,317	1.96±0.31	1.51±0.33	5.65±1.73	1.13±1.61	0.49±0.40	-0.99±0.03
Nares Gate	76	70	-1.15±0.40	1.19±0.27	-3.60±1.45	3.77±0.83	-	-

ature at the shelf break in each section is shown in Figure 8 C (POP) and F (HYCOM). On the whole the two simulations have a similar pattern of volume and heat fluxes. In both, the strongest on shelf flux is near the Denmark Strait, with weak on shelf flux north of the strait and mostly off shelf flux in western Greenland. The magnitudes of the fluxes and their variability differ between the two simulations. HYCOM has warmer water (panel F), with less variability in temperature compared to POP (panel C). Combined with stronger volume fluxes in HYCOM (panel D vs panel A) the result is greater magnitude heat fluxes in HYCOM (panel E vs B). While the HYCOM simulation does not have the same temporal variability as POP, there is along-transect variability where regions of strong off-shelf flux are adjacent to those with strong on-shelf flux. In POP, the temporal variability (shown here by the relative size of the 20th to 80th percentile range) is large relative to the mean between Sermilik Gate and the Denmark Strait. Topographic Rossby waves in this region could explain some of this variability, as discussed further in Section 4.3.

Table 2 summarizes the net heat and volume fluxes through every section and gate. The results from both HYCOM and POP simulations show that temperature within a given control volume is not closely linked to cross-isobath heat transport. This implies that shelf circulation and surface heat fluxes are important to the regional heat budget of the Greenland Continental Shelf. The results in Table 2 also indicate the role of the shelf circulation through the gate fluxes. The heat flux through the gates along the east coast of Greenland is southward. In both POP and HYCOM, there is less heat flux at Cape Farewell than at the Sermilik Gate indicating that the Narrow Shelf is a region of heat loss, despite it being a region of net on-shelf heat flux in HYCOM. Note Figure 4 shows the volume transport across the entire straits and should not be compared to these transports, which only include transport from the coast to the shelf contour.

In west Greenland, we expect to see off-shelf volume and heat transport in agreement with previous studies (e.g., Dukhovskoy et al., 2019; Böning et al., 2016; Schulze Chretien & Frajka-Williams, 2018; Myers et al., 2009). Both simulations are consistent in this region, with weak seasonal cycles of heat and volume transport. At the Davis Strait, the northward heat flux is small, and the northwest control volume is much colder than the southwest volume. The volume-averaged shelf temperature of the Southwest region is highly variable, and the fall peak is the warmest volume-average temperature of any region. The presence of warm ocean water in this region is consistent with observations of ocean-driven melting of the ice sheet in west Greenland (Holland et al., 2008). Cross-isobath heat transport is negative in the Southwest region, consistent with the source of heat to this region originating from southward heat transport at Cape Farewell or surface heat fluxes. Correlation between the heat flux at the Cape Farewell Gate and heat content in the Southwest region is 0.87 in POP and 0.74 in HYCOM; both are significant at a 95% confidence level. Using the surface heat flux time series saved from the POP simulation, we find that the net surface heat flux and heat content in the Southwest region are out of phase, resulting in low correlation. In both models, heat transport through the Cape Farewell Gate as well as the shelf temperature peak in the fall; in POP the net surface heat flux is maximum in the summer.

4.3 Daily Variability of Transport along the Greenland Shelf

Heat transport is also highly variable along the transect within the defined shelf regions and on multi-day timescales. Figures 9A and 10A show 5-month-long Hovmöller diagrams of temperature at 200 m in 2005 for each model at the shelf break, illustrating the seasonal progression of warm water from Denmark Strait to Davis Strait. To reduce noise in all variables from currents meandering across the isobath, a 50 km boxcar filter is applied. Hovmöller diagrams of 200 m temperature for the full five-year period are included in the supplemental material.

At the Denmark Strait there is a front between the cold Norwegian Seas water and the warm Atlantic water in the Irminger Current in both models, but the north part of the front is much colder in HYCOM (Figure 10A) consistent with the average shelf temperatures in both simulations (-0.62±0.17°C compared to 0.11±0.37°C in POP, see Table 2). The warmest water at the shelf break in both models is along the Wide Shelf region (between the Denmark and Sermilik Gates) and does not vary much seasonally. In POP between Sermilik Gate and Cape Farewell seasonal warming occurs in May (Figure 9). However, in HYCOM (Figure 10) the temperature over this portion of the shelf break shows more high-frequency variability than seasonal change. These differences are consistent with the annual cycles of temperature in the Southwest region and heat transport through the Cape Farewell and Davis Gates.

In both models, there is a high-frequency signal generated at or intersecting the shelf break south of the Denmark Strait in roughly the same location as the cold-warm

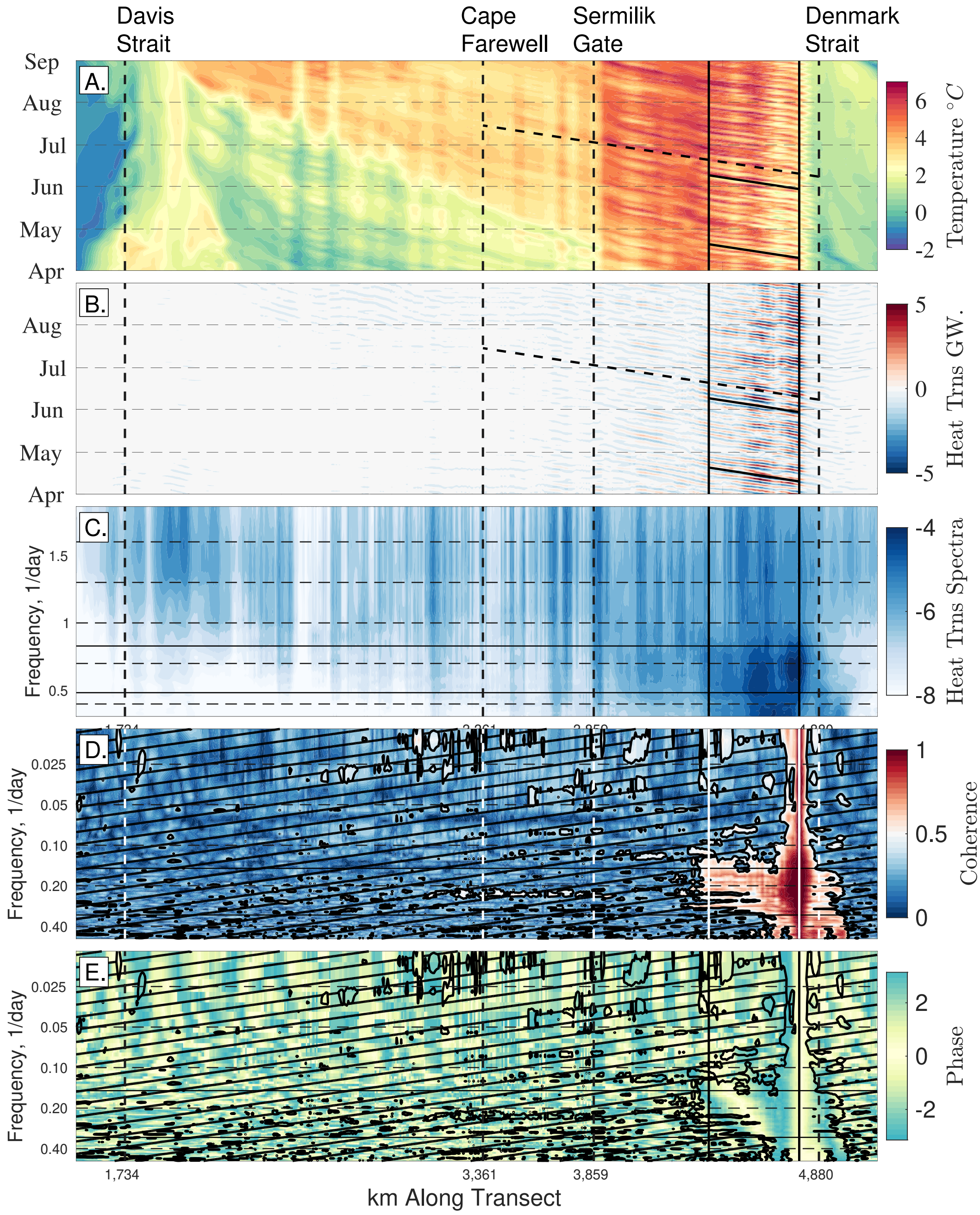

604 **Figure 9.** POP results showing:(A) Hovmöller diagrams from April to September 2005 of
605 temperature at 200 m, (B) vertically integrated heat transport with a 3-7 day band pass filter,
606 (C) spectra of heat transport at each location along the contour with horizontal lines showing
607 the frequency band that was used to produce (B), (D) coherence between heat transport at every
608 location and 90 km south of the Denmark Strait, and (E) the associated phase. Vertical dashed
609 lines show the locations of the gates, and solid vertical lines show the region of the propagating
610 signal from 90 to 500 km south of the Denmark Strait. Cross-hatching of coherence and phase
611 indicates that the coherence in not significant. Error for the spectra are estimated using a χ^2 dis-
612 tribution with a 95% significance level such that the range between high and low error estimates
613 is $\log_{10}(0.6)$.

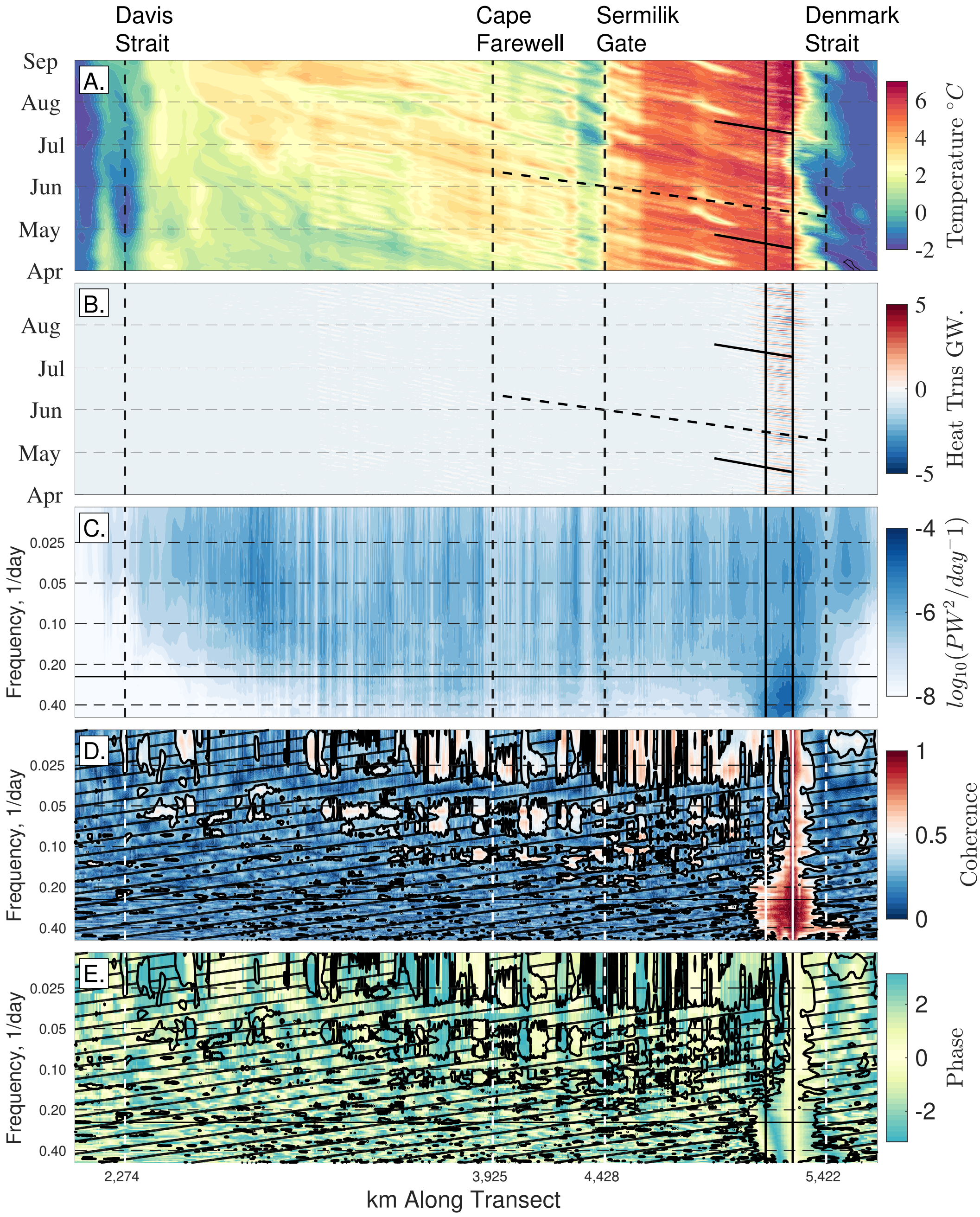

Figure 10. As in Figure 9. HYCOM results showing:(A) Hovmöller diagrams from April to September 2005 of temperature at 200 m, (B) vertically integrated heat transport with a 2-6 day band pass filter, (C) spectra of heat transport at each location along the contour with horizontal lines showing the frequency band that was used to produce (B), (D) coherence between heat transport at every location and 150 km south of the Denmark Strait, and (E) the associated phase. Vertical dashed lines show the locations of the gates, and solid vertical lines show the region of the propagating signal from 150 to 270 km south of the Denmark Strait. Cross-hatching of coherence and phase indicates that the coherence in not significant at the 95% level.

front (Figures 9A and 10A). In POP (Figure 9), the origin of these signals is consistently 90 km south of the Denmark Strait. In HYCOM (Figure 10) the position of the cold-warm front meanders and changes in strength over the months shown. These high-frequency signals are generated regularly throughout the year, including months not shown here. As these signals propagate along the transect they result in extreme high and low heat transports.

Figures 9B and 10B show the band-pass filtered vertically integrated heat transport, and Figures 9C and 10C show the spectra of the vertically integrated heat transport. In both models the heat transport spectra have peaks at high frequency south of the Denmark Strait. In POP (Figure 9), there are three localized regions of high-frequency variability, two with a frequency of about 0.30 day^{-1}, and one of higher frequency. In HYCOM (Figure 10) the high-frequency peak is more localized from 0.24 day^{-1} to 0.5 day^{-1}, the Nyquist frequency. Therefore, to isolate the heat transport associated with these propagating signals, the models were band-pass filtered with different ranges: for POP the range is a period of 3-7 days, and for HYCOM the range is 2-4 days. The band-pass filtered heat transport in both models (Figures 9(B) and 10(B)) shows a propagating signal, though the signal travels only 120 km in HYCOM, while in POP it continues for 410 km. The location where the signal dissipates in HYCOM (Figure 10) coincides with the mouth of Kangerdlugssuaq Trough. In POP (Figure 9) the signal dissipates on the north end of the Sermilik Troughs. In both cases the dissipation or on/off-shelf shifting of the signal occurs where there is a change in bathymetry. In both models (Figures 9C and 10C), the high-frequency energy in the spectra of vertically integrated heat transport decays southward along the shelf. From Sermilik Gate to Davis Strait, much of the variability in both models is at frequencies below 0.15 day^{-1}. In HYCOM (Figure 10), the energy in that range is consistent over that portion of the shelf break; however, in POP (Figure 9) there are regions of very low spectral energy especially where the winds are weakest.

The coherence of heat transport time series at each location along the contour and the heat transport at the origin location of the signals, with the associated phase, was used to assess these signals; Figures 9D and 10D show the coherence squared, and Figures 9E and 10E show the associated phase. Where the coherence squared is less than the 95% confidence level $\Gamma^2_{XY} = 0.39$, coherence and phase are hatched. For both models, there are regions of strong coherence both north (upstream, closer to the Denmark

Strait) and south (downstream, farther from the Denmark Strait). The upstream coherence shows the possible origin of the signal. In HYCOM (Figure 10) the coherence is significant north of the Denmark Strait in the same narrow high-frequency band (0.24-0.5 day^{-1}). In POP (Figure 9) the coherence is significant north of the Denmark Strait across most frequencies in the 3-7 day band. The fact that the forcing differs could potentially explain the differences in the coherent responses.Both the model bathymetry and the choice of shelf break contours could also contribute to the difference. In both models, where the coherence is significant south of the Denmark Strait, the phase shows evidence of a propagating signal. In HYCOM, there is also coherence at low frequencies along the shelf to Cape Farewell and partway along the western Greenland shelf. This coherent signal is not present in POP and could be related to the larger scale meandering of the front where the signal originates, or any of the differences in model set up listed above that could explain differences in the high frequency signals, but thorough analysis is beyond the scope of this study.

As in Figures 9C and 10C, the frequencies where the signals are coherent along the transect (from right to left in Figures 9 and 10) differ between simulations. From the phase, we can estimate the phase velocity of the signal (Münchow et al., 2020; Pickart & Watts, 1990). A middle frequency of each band of coherence was used, f_{POP}=0.2 day^{-1} for POP and f_{HYCOM}=0.34 day^{-1} for HYCOM. A location was chosen along the contour near where the coherence at that frequency is no longer significant, 500 km south of the Denmark Strait in POP, 270 km in HYCOM; the distance between the two locations is D. At that frequency and location, the phase is $\Theta_{XY} = 128°$ in POP and $\Theta_{XY} = 52°$ in HYCOM. We calculate the phase speed as $c_p = f(360/\Theta_{XY})(D/\cos\Delta)$, where Δ is the angle between the wavenumber vector and the direction of the shelf break. In this region, the difference in the direction of the average velocity and shelf break direction was used to estimate Δ, with $\Delta = 4°$ in POP and $\Delta = 14°$ in HYCOM. For POP, the resulting phase velocity is $c_p = 2.6$ m/s and wave length $\lambda = 1,155$ km; for HYCOM, the resulting phase velocity is $c_p = 3.3$ m/s and wave length $\lambda = 863$ km. The spectra, coherence, and phase used for estimating the phase velocity are shown in the Supplemental Material.

In addition, we use the dispersion relation for topographic Rossby waves

$$\omega = \frac{N\alpha\sin(\phi)}{\tanh(KL_D)} \tag{5}$$

to estimate the orientation of the wavenumber vector, $\phi = k/K$ where $\vec{k} = (k, l)$ and $K = \sqrt{k^2 + l^2}$. The stability frequency N is estimated from profiles of the 5-year average stratification in this region of the shelf, $N = 0.003$ s^{-1} in POP and 0.002 s^{-1} in HYCOM. The average bottom slope estimated from the change in local bathymetry to be $\alpha = 0.02$ for POP and HYCOM. The Rossby radius of deformation $L_S = ND/f$ is calculated at each point along the contour, using the local depth and Coriolis parameter, the average value of $L_D = 12$ km in this region of both models. For POP, using this equation and the estimated wavelength from the phase analysis, the value of $\phi = 1°$, compared to the orientation of the current ellipse at the shelf break $\theta = -6°$. In HYCOM, the angle of the wavenumber vector is $\phi = 4°$, and the average direction orientation of the current ellipse is $\theta = -0.5°$. This agreement between the direction of wave propagation estimated from the topographic Rossby waves dispersion relationship and the velocity elipses at the shelf break is consistent with the hypothesis that these waves are topographic Rossby waves.

These waves are present in both the vertically integrated heat transport and the 200 m temperature. In the previous section, we showed that offshore Ekman transport was not the leading mechanism of heat transport in this region. Because of the strength of the propagating signal across all depths in this region, we hypothesize it to be the primary mechanism of cross-shelf exchange. The mean heat transport in this region in Figure 8 over the five years of our study period is highly variable but has a net on-shelf transport. Therefore, we conclude that these waves not only perturb the thermocline but also result in a net heat transport onto the shelf.

5 Discussion

Our goal is to better understand the heat budget of the shelf, and the mechanisms governing heat transport. From the observed heat transports, we find variability on two timescales. On the seasonal scale, warming of the shelf is associated both with cross-shelf transports and with the transport of heat by currents on the shelf. On shorter time scales, there is evidence that topographic Rossby waves propagate from south of the Denmark Strait to locations along the shelf where the bathymetry changes rapidly. For the seasonal variability of volume and heat transport, the role of winds through Ekman transport is proposed as a leading mechanism. For the waves, the local and regional winds are investigated as a source of the high-frequency signals. Together, these mechanism

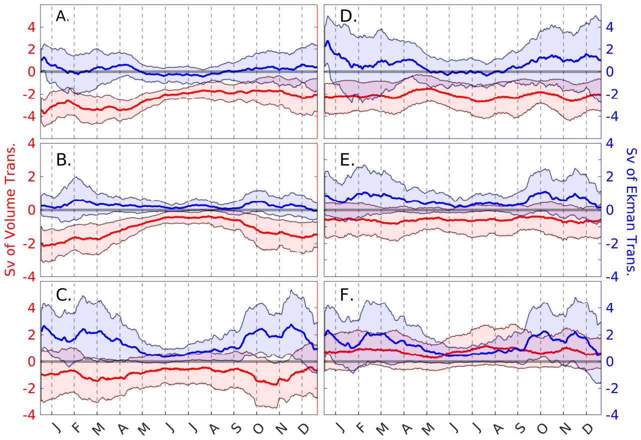

Figure 11. Comparison of the mean of the daily Ekman transport (Sv, blue) to net cross-isobath volume transports (Sv, red) from 2005-2009 in three focus regions: Southwest (A,D), Narrow Shelf (B,E), and Wide Shelf (C, F). (A-C) are results from POP and CORE-IAF, (D-F) are results from HYCOM and CFSR. Time series are smoothed with a 30-day running mean; shaded areas show the 20th and 80th percentile range for each day. Transports are positive shoreward.

set the boundary conditions of the continental shelf heat budget. The combination of both mechanisms controls the heat flux in the shelf region where there is strongest shoreward heat flux. The connection between the mechanisms and the heat budget is essential to understanding shelf temperature sensitivity to large scale changes.

5.1 Mechanism One: Ekman Dynamics

Winds in southeast Greenland are predominantly downwelling favorable near the coast and along the shelf break. Northerly winds drive Ekman transport that advects surface water onto the shelf setting up a strong sea surface gradient and driving downwelling, forcing deeper water off the shelf. Using the net surface stress (including both winds and sea ice), we can estimate the resulting Ekman transport across our selected transect. We define the net Ekman downwelling transport (m^3 s^{-1}) across a given section of the 800 m isobath as

$$V_{DW} = \int_0^L \frac{1}{f\rho}\tau_{along}dx, \tag{6}$$

where ρ is the density of sea water (not property dependent), and f is the Coriolis parameter, which varies with latitude.

We also consider whether differences in the two forcing products (CORE-IAF for POP and CFSR for HYCOM) may influence the transport in both simulations. We expect that, in two atmospherically forced simulations with robust physics, transport mechanisms would agree; however, we must consider how differences in the forcing could produce different dynamics. To quantify this, in the most basic way, we use linear regression to compare the difference of the Ekman transports $V_{DW\ diff} = V_{DW-HYCOM} - V_{DW-POP}$ and the difference in volume transports $V_{800\ diff} = V_{800-HYCOM} - V_{800-POP}$.

In Figure 11, time series of V_{DW} and V_{800} are plotted for three different regions: Southwest, Narrow Shelf, and Wide Shelf; positive transports are onto the shelf. The differences in V_{DW} estimated from POP and HYCOM highlight the differences in the wind forcing. The mean annual cycle illustrates the seasonality of the wind forcing and cross-isobath transports, with the acknowledgement that by using only five years of data, year-to-year variability is still present. Vertical profiles of volume fluxes in the Narrow and Wide Shelf regions have shown that while the net volume transport is off the shelf, there is onshore flux near the surface (upper 250 m). In the Southwest region, the volume transport is generally off the shelf over the entire water column.

In the Southwest region (panels A and D), the surface forcing in both models drives seasonally varying on-shelf (winter) and off-shelf (summer) Ekman transports. Dukhovskoy et al. (2019) argued that variability in the along-isobath winds explains 67% of variability in the off-shelf transport of fresh water on the southwestern Greenland Shelf. In HYCOM, the winds, and the resulting Ekman transport, are stronger and show a larger range of variability when compared to POP. While the POP volume transport varies seasonally, the HYCOM transport does not display the same seasonality. The difference in transport variability timescale (seasonal in POP and year-to-year in HYCOM) could be one reason that the 2005-2009 average transports differ between the models. In this region, surface forcing plays a larger role in influencing cross-shelf transports in POP compared to HYCOM. In comparing the difference in Ekman transport to the difference in net volume transport, we find the Southwest region to have the strongest relationship of any of the sections listed here, with $V_{DW\ diff}$ explaining 5% of the variance in $V_{800\ diff}$.

Over the Narrow Shelf (panels B and E), the difference in wind stress between the two atmospheric reanalysis products is apparent. The transport from surface stress in POP is small when compared to the cross-isobath volume transport. In both simulations, the seasonal cycle is consistent with strengthening of the along-shelf winds in winter. The stronger onshore transport in HYCOM is consistent with the stronger winds in CFSR (HYCOM, see Figure 6). This difference in transport could be linked to a difference in model forcing or atmosphere-ocean coupling, not model dynamics. The cross-isobath volume transport varies seasonally in POP, but in HYCOM it has a consistent magnitude throughout the year; this is similar to the difference between the two simulations in the Southwest region and consistent with the hypothesis that cross-isobath transport is wind driven.

Over the Wide Shelf (panels C and F), the mean and variability of Ekman transport are similar between the two forcings. However, the cross-isobath transports have different signs. Note, this is the region in both models where the topographic Rossby waves propagate, with impacts on both volume and heat transport. In POP the variability of the volume transport resembles the Ekman transport, but with opposite sign as has been the case in the other shelf regions. In HYCOM, the transport is consistently onto the shelf, in agreement with the Ekman transport. The topographic Rossby waves traveling along the shelf break in this region are likely wind-generated, as discussed in the next section, and influence the volume transport onto the shelf.

Overall, to understand where winds drive cross-isobath transport, we look at the regions in both simulations where the transports are correlated to the winds. In the Southwest region, along-isobath winds explain similar amounts of variance in POP (6%) and HYCOM (5%). In HYCOM, neither wind forcing explains more that 1% of the variance in transport over the Narrow or Wide Shelf. However, in POP Ekman convergence in the Narrow Shelf region explained 32% of variance in cross-isobath volume transport; no other region had a similar correlation to Ekman convergence. In both simulations, we found that along the Southeast shelf the off-shelf volume transport was the result of relatively weak onshore fluxes being compensated by stronger offshore fluxes at depth. Combined with the low correlation to Ekman transport we conclude that the cross-isobath exchange does not occur primarily in the Ekman layer. These results differ from previous results linking along-shelf winds to off-shelf transport of freshwater in southwest Greenland (Dukhovskoy et al., 2019). We attribute this to the vertical distribution of freshwater, which is concentrated in the surface layer and directly influenced by Ekman transport. In addition, while there are some differences in the wind forcing between simulations, the connection between the winds and the transport is not strong enough in ei-

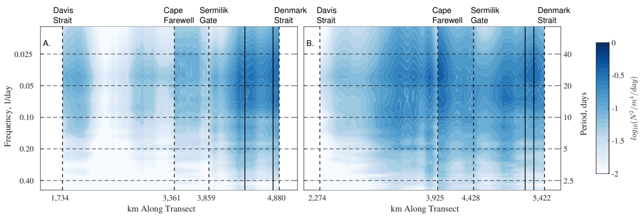

Figure 12. Plots of spectra computed from daily fields projected net surface stress at every point along the transect from Denmark Strait to Davis Strait. (A) is results from POP-CORE-IIAF, (B) is results from HCYOM - CFSR. Vertical dashed lines show the locations of the gates and solid vertical lines show the region of the propagating signal. In (A) the range of the black bars is 90 to 500 km for (B) is is from 150 to 270 km, both referenced to the Denmark Strait

ther simulation to suggest that differences in forcing products are the primary cause of differences between the two simulations. This is further evidence that Ekman transport is not a primary driver of cross-shelf transport in these regions.

5.2 Mechanism Two: Wind Generation of Topographically Trapped Rossby Waves

In the Hovmöller diagrams (Figures 9A and 10A) we observed high-frequency signals that emanated from a location south of the Denmark Strait. These signals are comparable to the topographically trapped Rossby waves (Münchow et al., 2020) in a trough near the Fram Strait, to the cyclonic eddies formed at the Denmark Strait (Moritz et al., 2019), and to the coastally trapped shelf waves in this region (Gelderloos et al., 2021). The period, high phase velocity, and wavelength are more consistent with topographic Rossby waves than with Kelvin waves or gravity waves. In earlier studies, wind forcing has been proposed as the primary mechanism that produces similar high frequency signals (Gelderloos et al., 2021). We focus on the local winds at the shelf break and use frequency spectra (Figure 12) to determine if the frequency of the local winds matches the frequency of the waves, although the winds do not need to have the frequency of the signal that they generate. However, this does not exclude the possibility of wind forcing, Dukhovskoy, Morey, and O'Brien (2009) found tropical storms generated by low-frequency waves along the Nicaragua Shelf.

Spectra are calculated at each point along the shelf break using the winds projected onto the along-isobath direction for each of the three main regions: Southwest, Narrow Shelf, and Wide Shelf. Both wind products show the most variability around 0.05 day^{-1}. The low spatial resolution of both wind products (approximately 90 km for CORE-IAF and approximately 38 km for CFSR) results in the reduced along-shelf variability seen in the spectra; compare to panel C in Figures 9 and 10 where spectra at nearby locations vary. The strong winds over the Narrow Shelf in the HYCOM forcing are likely connected to the relatively greater energy in the surface stress near Cape Farewell. At the location along the transect where the signals are generated there is not a clear corresponding high-frequency signal in the surface forcing. However, the volume transport at the location of generation is correlated with the surface stress across the region. This provides evidence that the topographic Rossby waves are generated remotely rather than at the shelf break.

Comparing the portion of the shelf along which the waves propagate to the spatial patterns of EKE in both simulations (Figure 3), we identify regions where the topographic Rossby waves may be generated. The elevated EKE extends north of the Denmark Strait in both simulations to the mouth of Scoresby Sound. In HYCOM, the band of high EKE extends unbroken across the Denmark Strait and is shoreward of the 800 m isobath south of the strait. If we consider the region of elevated EKE to be a proxy for the path of the topographic Rossby waves, this would indicate one reason they are not apparent in HYCOM south of Kangerdlugssuaq Trough is because they are further onshore than the 800 m bathymetric contour. In POP, the shoreward shifting of the band of elevated EKE occurs further south, consistent with the along-shelf propagation of the topographic Rossby waves. Furthermore, the pattern of elevated EKE indicates these waves could be remotely generated as far north along the shelf as Scoresby Sound. Further investigation of the generation of these waves is beyond the scope of this work.

6 Conclusion

In order to assess the heat transport onto the Greenland Continental Shelf, we compared in detail two high-resolution coupled ocean-sea ice simulations with different atmospheric forcing. Using a control volume around the 800 m isobath and gates at key locations on the shelf, we determine not only how much heat crosses onto the shelf but also the patterns of transport on the shelf. The region of greatest heat transport onto the shelf is between the Denmark Strait and the Sermilik Troughs in southeast Greenland, where the average heat transport is 16.4±13.8 TW in POP and 55.0±23.3 TW in HYCOM. Currents on the shelf are important in spreading warm water to different shelf regions; in both models the primary source of heat on the southwest continental shelf is from southward transport through the Cape Farewell Gate. The warmest part of the shelf is between the Denmark Strait and the Davis Strait; this region also has the largest seasonal change in heat content.

In this study we hypothesised wind-driven transports as one driver of heat transport onto the shelf, but volume transport was not clearly linked to off-shore Ekman transport. In none of our shelf regions did Ekman dynamics appear to be the primary driver of cross-isobath transport. However, the vertical distribution analyses show that transport in the upper layer is compensated by much stronger off-shelf transport at depth. We also quantified how differences in the surface wind stress from our atmospheric forcings contributed to the differences in cross shelf transport and found that the wind forcings could not explain the difference.

Topographic Rossby waves propagate along the shelf break, originating south of the Denmark Strait. These waves have periods of 3-7 days and propagate along the section of the shelf with the strongest on-shelf volume and heat fluxes. The transport associated with these waves is key in our budget of the Greenland Shelf. They appear to be the leading mechanism of cross shelf exchange and result in a net heat transport onto the shelf. Their occurrence in both simulations indicates that their presence is robust. Similar waves have been observed in other high-resolution simulations. In our simulations, local winds do not appear to be a critical driver of wave generation. Further study is needed to identify the key mechanisms including observations that would show evidence of these waves.

At the outset of this project, our premise for comparing these simulations was that they would provide independent realizations of the Greenland Current system and that the dominant dynamics would be apparent, regardless of model design, if each of the models was reasonably realistic. Both models are similar to observations and to each other in terms of surface currents and EKE, basin temperature and salinity, and volume transport through major straits. Fully understanding what difference in the simulation setup results in the difference in dynamics is beyond the scope of this work; however, we hypothesize that the primary drivers of differences between the two simulated transports stem from the use of different atmospheric forcings and resolution, and that differing vertical coordinate systems could have contributed. Our key findings are consistent between the two simulations despite differences in properties on the shelf and in cross-shelf exchange.

One aspect of the dynamics of the Greenland continental shelf that has been neglected in this study is the role of ice sheet meltwater in these cross-shelf exchange mechanisms. Neither simulation includes a representation of GIS meltwater, which is expected to modify vertical and horizontal shelf stratification. Further simulations are needed to explore the implications of accelerated melting on shelf warming. In addition, our study has shown that mesoscale processes contribute to on-shelf transport. High-resolution studies in this region are needed to understand these processes. Such high-resolution studies could also address the dynamics between the shelf break and the ice sheets that bring the warm water we observe crossing the shelf to the front of glaciers where it drives melting.

Acknowledgments

T.J. Morrison, J.L. McClean and S.T. Gille were funded by DOE Office of Science grants: DE-SC0014440 and DE-SC0020073. D. Dukhovskoy and E.Chassignet were funded by the DOE award DE-SC0014378 and HYCOM NOPP (award N00014-15-1-2594). The HYCOM-CICE simulations were supported by a grant of computer time from the DoD High-Performance Computing Modernization Program at NRL SSC. The POP/CICE simulation was run with a National Center for Atmospheric Research Climate Simulation Laboratory (CSL) allocation on Yellowstone (ark:/85065/d7wd3xhc), sponsored by the National Science Foundation. Some POP/CICE analyses were carried out using Rhea in the Oak Ridge Leadership Computing Facility at the Oak Ridge National Laboratory. We thank Mathew Maltrud (LANL) for preparing the sea-ice initial condition used in the POP/CICE simulation. We thank André Palóczy for advice on the calculation of heat fluxes in POP.

References

An, L., Rignot, E., Chauche, N., Holland, D. M., Holland, D., Jakobsson, M., ... others (2019). Bathymetry of southeast greenland from oceans melting greenland (omg) data. *Geophysical Research Letters*, *46*(20), 11197–11205.

Arzeno-Soltero, I. B., Giddings, S. N., Pawlak, G., McClean, J. L., Wang, H., Rainville, L., & Lee, C. M. (2021). Generation of low-latitude seamount-trapped waves: A case study of the seychelles plateau. *Journal of Geophysical Research: Oceans*, *126*(8), e2021JC017234.

Bacon, S., & Fofonoff, N. (1996). Oceanic heat flux calculation. *J. Atmos. Ocean. Tech.*, *13*, 1327–1329. doi: 10.1175/1520-0426(1996)013⟨1327:OHFC⟩2.0.CO;2

Benn, D. I., Cowton, T., Todd, J., & Luckman, A. (2017). Glacier calving in Greenland. *Current Climate Change Reports*, *3*(4), 282–290.

Beszczynska-Moeller, A., Woodgate, R. A., Lee, C., Melling, H., & Karcher, M. (2011). A synthesis of exchanges through the main oceanic gateways to the Arctic Ocean. *Oceanography*, *24*(3), 82–99.

Bitz, C. M., & Lipscomb, W. H. (1999). An energy-conserving thermodynamic model of sea ice. *Journal of Geophysical Research: Oceans*, *104*(C7), 15669–15677.

Bleck, R. (2002). An oceanic general circulation model framed in hybrid isopycnic-Cartesian coordinates. *Ocean modelling*, *4*(1), 55–88.

Böning, C. W., Behrens, E., Biastoch, A., Getzlaff, K., & Bamber, J. L. (2016). Emerging impact of Greenland meltwater on deepwater formation in the North Atlantic Ocean. *Nature Geoscience*, *9*(7), 523–527.

Brandt, P., Schott, F. A., Funk, A., & Martins, C. S. (2004). Seasonal to interannual variability of the eddy field in the Labrador Sea from satellite altimetry. *Journal of Geophysical Research: Oceans*, *109*(C2).

Briegleb, P., & Light, B. (2007). *A Delta-Eddington mutiple scattering parameterization for solar radiation in the sea ice component of the community climate system model* (Tech. Rep. Nos. NCAR/TN-472+STR). University Corporation for Atmospheric Research. doi: 10.5065/D6B27S71

Castillo-Trujillo, A. C., Arzeno-Soltero, I. B., Giddings, S. N., Pawlak, G., McClean, J., & Rainville, L. (2021). Observations and modeling of ocean circulation in the Seychelles Plateau Region. *Journal of Geophysical Research: Oceans*, *126*(2), e2020JC016593.

Chassignet, E. P., Hurlburt, H. E., Metzger, E. J., Smedstad, O. M., Cummings, J., Halliwell, G. R., . . . Wilkin, J. (2009). Global ocean prediction with the

HYbrid Coordinate Ocean Model (HYCOM). *Oceanography*, *22*(2), 64-75.

Chassignet, E. P., Hurlburt, H. E., Smedstad, O. M., Halliwell, G. R., Hogan, P. J., Wallcraft, A. J., ... Bleck, R. (2007). The HYCOM (HYbrid Coordinate Ocean Model) data assimilative system. *Journal of Marine Systems*, *65*(1-4), 60–83.

Chassignet, E. P., Smith, L. T., Halliwell, G. R., & Bleck, R. (2003). North atlantic simulations with the HYbrid Coordinate Ocean Model (HYCOM): Impact of the vertical coordinate choice, reference density, and thermobaricity. *Journal of Physical Oceanography*, *33*, 2504–2526.

Christoffersen, P., O'Leary, M., Van Angelen, J. H., & Van Den Broeke, M. (2012). Partitioning effects from ocean and atmosphere on the calving stability of Kangerdlugssuaq Glacier, East Greenland. *Annals of Glaciology*, *53*(60), 249–256.

Craig, A. P., Vertenstein, M., & Jacob, R. (2012). A new flexible coupler for Earth system modeling developed for CCSM4 and CESM1. *The International Journal of High Performance Computing Applications*, *26*(1), 31–42.

Cuny, J., Rhines, P. B., & Kwok, R. (2005). Davis Strait volume, freshwater and heat fluxes. *Deep Sea Research Part I: Oceanographic Research Papers*, *52*(3), 519–542.

Curry, B., Lee, C., & Petrie, B. (2011). Volume, freshwater, and heat fluxes through Davis Strait, 2004–05. *Journal of Physical Oceanography*, *41*(3), 429–436.

Curry, B., Lee, C. M., Petrie, B., Moritz, R. E., & Kwok, R. (2014). Multiyear volume, liquid freshwater, and sea ice transports through Davis Strait, 2004–10. *Journal of Physical Oceanography*, *44*(4), 1244–1266.

De Steur, L., Peralta-Ferriz, C., & Pavlova, O. (2018). Freshwater export in the east Greenland current freshens the North Atlantic. *Geophysical Research Letters*, *45*(24), 13–359.

Dinniman, M. S., Klinck, J. M., & Smith Jr, W. O. (2011). A model study of Circumpolar Deep Water on the West Antarctic Peninsula and Ross Sea continental shelves. *Deep Sea Research Part II: Topical Studies in Oceanography*, *58*(13-16), 1508–1523.

Dukhovskoy, D. S., Chassignet, E. P., Hogan, P. J., Metzger, E. J., Posey, P., Smedstad, O. M., ... Wallcraft, A. J. (2016). Current state and recent changes in the Arctic Ocean from the HYCOM-NCODA global ocean and sea ice prediction system. In *Agu fall meeting abstracts* (Vol. 2016, pp. GC23H–07).

Dukhovskoy, D. S., Morey, S. L., & O'Brien, J. J. (2009). Generation of baroclinic topographic waves by a tropical cyclone impacting a low-latitude continental shelf. *Continental Shelf Research*, *29*(1), 333–351.

Dukhovskoy, D. S., Yashayaev, I., Chassignet, E. P., Meyers, P. G., Platov, G., & Proshutinsky, A. (2021). Time scales of the Greenland Freshwater Anomaly in the Subpolar North Atlantic. *Journal of Climate*.

Dukhovskoy, D. S., Yashayaev, I., Proshutinsky, A., Bamber, J., Bashmachnikov, I., Chassignet, E., ... Tedstone, A. (2019). Role of greenland freshwater anomaly in the recent freshening of the subpolar north atlantic. *Journal of Geophysical Research: Oceans*, *124*(5), 3333–3360.

Dukowicz, J. K., & Smith, R. D. (1994). Implicit free-surface method for the Bryan-Cox-Semtner ocean model. *Journal of Geophysical Research: Oceans*, *99*(C4), 7991–8014.

Dushaw, B. D., & Sagen, H. (2016). A comparative study of moored/point and acoustic tomography/integral observations of sound speed in Fram Strait using objective mapping techniques. *Journal of Atmospheric and Oceanic Technology*, *33*(10), 2079–2093.

Fratantoni, D. M. (2001). North Atlantic surface circulation during the 1990's observed with satellite-tracked drifters. *Journal of Geophysical Research: Oceans*, *106*(C10), 22067–22093.

Furevik, T., & Nilsen, J. E. Ø. (2005). Large-scale atmospheric circulation variability and its impacts on the Nordic Seas ocean climate—A review. In *The nordic seas: An integrated perspective* (p. 105-136). American Geophysical Union (AGU). doi: 10.1029/158GM09

Gelderloos, R., Haine, T. W., & Almansi, M. (2021). Coastal trapped waves and other subinertial variability along the Southeast Greenland Coast in a realistic numerical simulation. *Journal of Physical Oceanography*, *51*(3), 861–877.

Gillard, L. C., Hu, X., Myers, P. G., Ribergaard, M. H., & Lee, C. M. (2020). Drivers for atlantic-origin waters abutting greenland. *The Cryosphere*, *14*(8), 2729–2753.

Goddard, P. B., Dufour, C. O., Yin, J., Griffies, S. M., & Winton, M. (2017). CO_2-

induced ocean warming of the antarctic continental shelf in an eddying global climate model. *Journal of Geophysical Research: Oceans*, *122*(10), 8079–8101.

Gouretski, V., & Koltermann, K. P. (2004). WOCE global hydrographic climatology. *Berichte des BSH*, *35*, 1–52.

Hanna, E., Jones, J. M., Cappelen, J., Mernild, S. H., Wood, L., Steffen, K., & Huybrechts, P. (2013). The influence of North Atlantic atmospheric and oceanic forcing effects on 1900–2010 Greenland summer climate and ice melt/runoff. *International Journal of Climatology*, *33*(4), 862–880.

Håvik, L., Våge, K., Pickart, R. S., Harden, B., Appen, W.-J. v., Jónsson, S., & Østerhus, S. (2017). Structure and variability of the shelfbreak East Greenland Current north of Denmark Strait. *Journal of Physical Oceanography*, *47*(10), 2631–2646.

Holland, D. M., Thomas, R. H., De Young, B., Ribergaard, M. H., & Lyberth, B. (2008). Acceleration of Jakobshavn Isbrae triggered by warm subsurface ocean waters. *Nature geoscience*, *1*(10), 659.

Holliday, N. P., Bacon, S., Cunningham, S. A., Gary, S. F., Karstensen, J., King, B. A., … McDonagh, E. L. (2018). Subpolar North Atlantic overturning and gyre-scale circulation in the summers of 2014 and 2016. *Journal of Geophysical Research: Oceans*, *123*(7), 4538–4559.

Howat, I. M., Smith, B. E., Joughin, I., & Scambos, T. A. (2008). Rates of southeast Greenland ice volume loss from combined ICESat and ASTER observations. *Geophysical Research Letters*, *35*(17).

Hunke, E., & Dukowicz, J. (1997). An elastic–viscous–plastic model for sea ice dynamics. *Journal of Physical Oceanography*, *27*(9), 1849–1867.

Hunke, E. C., Lipscomb, W. H., Turner, A. K., Jeffery, N., & Elliott, S. (2010). Cice: the los alamos sea ice model documentation and software user's manual version 4.1 la-cc-06-012. *T-3 Fluid Dynamics Group, Los Alamos National Laboratory*, *675*.

Hurrell, J. W., Holland, M. M., Gent, P. R., Ghan, S., Kay, J. E., Kushner, P. J., … others (2013). The Community Earth System Model: A framework for collaborative research. *Bulletin of the American Meteorological Society*, *94*(9), 1339–1360.

Jackson, R. H., Straneo, F., & Sutherland, D. A. (2014). Externally forced fluctuations in ocean temperature at Greenland glaciers in non-summer months. *Nature Geoscience*, *7*(7), 503.

Jochumsen, K., Quadfasel, D., Valdimarsson, H., & Jónsson, S. (2012). Variability of the Denmark Strait overflow: Moored time series from 1996–2011. *Journal of Geophysical Research: Oceans*, *117*(C12).

Large, W. G., McWilliams, J. C., & Doney, S. C. (1994). Oceanic vertical mixing: A review and a model with a nonlocal boundary layer parameterization. *Reviews of Geophysics*, *32*(4), 363–403.

Large, W. G., & Yeager, S. (2009). The global climatology of an interannually varying air–sea flux data set. *Climate dynamics*, *33*(2-3), 341–364.

Le Bras, I. A.-A., Straneo, F., Holte, J., & Holliday, N. P. (2018). Seasonality of freshwater in the east Greenland current system from 2014 to 2016. *Journal of Geophysical Research: Oceans*, *123*(12), 8828–8848.

Luthcke, S. B., Zwally, H. J., Abdalati, W., Rowlands, D. D., Ray, R. D., Nerem, R. S., … Chinn, D. S. (2006). Recent Greenland ice mass loss by drainage system from satellite gravity observations. *Science*, *314*(5803), 1286–1289.

McClean, J. L., Bader, D. C., Bryan, F. O., Maltrud, M. E., Dennis, J. M., Mirin, A. A., … Worley, P. H. (2011). A prototype two-decade fully-coupled fine-resolution CCSM simulation. *Ocean Modelling*, *39*(1-2), 10-30. doi: 10.1016/j.ocemod.2011.02.011

McClean, J. L., Bader, D. C., Maltrud, M. E., Evans, K. J., Taylor, M., Tang, Q., … Mahajan, S. (2018). High-resolution fully-coupled ACME v0.1 approximate present day transient climate simulations.. (Ocean Sciences Meeting 2018, 12-16/February, Portland/OR. Abstract ID: OM44C-2143.)

Meehl, G. A., Stocker, T. F., Collins, W. D., Friedlingstein, P., Gaye, T., Gregory, J. M., … Zhao, Z. C. (2007). Global climate projections. In S. Solomon et al. (Eds.), *Climate change 2007: The physical science basis. contribution of Working Group I to the Fourth Assessment Report of the Intergovernmental Panel on Climate Change.* Cambridge, United Kingdom and New York, NY, USA: Cambridge University Press.

Metzger, E. J., Smedstad, O. M., Thoppil, P. G., Hurlburt, H. E., Cummings, J. A., Wallcraft, A. J., … others (2014). US Navy operational global ocean and Arctic ice prediction systems. *Oceanography*, *27*(3), 32–43.

Millan, R., Rignot, E., Mouginot, J., Wood, M., Bjørk, A. A., & Morlighem, M. (2018). Vulnerability of Southeast Greenland glaciers to warm Atlantic water from Operation IceBridge and Ocean Melting Greenland data. *Geophysical Research Letters*.

Moritz, M., Jochumsen, K., North, R. P., Quadfasel, D., & Valdimarsson, H. (2019). Mesoscale eddies observed at the Denmark Strait sill. *Journal of Geophysical Research: Oceans*, *124*(11), 7947–7961.

Morlighem, M., Williams, C. N., Rignot, E., An, L., Arndt, J. E., Bamber, J. L., ... others (2017). BedMachine v3: Complete bed topography and ocean bathymetry mapping of Greenland from multibeam echo sounding combined with mass conservation. *Geophysical research letters*, *44*(21).

Mouginot, J., Rignot, E., Bjørk, A. A., van den Broeke, M., Millan, R., Morlighem, M., ... Wood, M. (2019). Forty-six years of Greenland Ice Sheet mass balance from 1972 to 2018. *Proceedings of the National Academy of Sciences*, 201904242.

Münchow, A., & Melling, H. (2008). Ocean current observations from Nares Strait to the west of Greenland: Interannual to tidal variability and forcing. *Journal of Marine Research*, *66*(6), 801–833.

Münchow, A., Melling, H., & Falkner, K. K. (2006). An observational estimate of volume and freshwater flux leaving the Arctic Ocean through Nares Strait. *Journal of Physical Oceanography*, *36*(11), 2025–2041.

Münchow, A., Schaffer, J., & Kanzow, T. (2020). Ocean circulation connecting fram strait to glaciers off northeast greenland: Mean flows, topographic rossby waves, and their forcing. *Journal of Physical Oceanography*, *50*(2), 509–530.

Murray, R. J. (1996). Explicit generation of orthogonal grids for ocean models. *Journal of Computational Physics*, *126*(2), 251–273.

Myers, P. G., Donnelly, C., & Ribergaard, M. H. (2009). Structure and variability of the West Greenland Current in summer derived from 6 repeat standard sections. *Progress in Oceanography*, *80*(1-2), 93–112.

Nurser, A., & Bacon, S. (2014). The Rossby radius in the Arctic Ocean. *Ocean Science*, *10*(6), 967–975.

Palóczy, A., Gille, S. T., & McClean, J. L. (2018). Oceanic heat delivery to the Antarctic Continental Shelf: Large-scale, low-frequency variability. *Journal of*

Geophysical Research: Oceans, *123*(11), 7678–7701.

Palóczy, A., McClean, J. L., Gille, S. T., & Wang, H. (2020). The large-scale vorticity balance of the Antarctic continental margin in a fine-resolution global simulation. *Journal of Physical Oceanography*, *50*(8), 2173–2188.

Pickart, R. S., & Watts, D. R. (1990). Deep western boundary current variability at Cape Hatteras. *Journal of Marine Research*, *48*(4), 765–791.

Rignot, E., Fenty, I., Menemenlis, D., & Xu, Y. (2012). Spreading of warm ocean waters around Greenland as a possible cause for glacier acceleration. *Annals of Glaciology*, *53*(60), 257–266.

Rossby, T., Flagg, C., Chafik, L., Harden, B., & Søiland, H. (2018). A direct estimate of volume, heat, and freshwater exchange across the Greenland-Iceland-Faroe-Scotland Ridge. *Journal of Geophysical Research: Oceans*, *123*(10), 7139–7153.

Saha, S., Moorthi, S., Pan, H.-L., Wu, X., Wang, J., Nadiga, S., ... others (2010). The NCEP climate forecast system reanalysis. *Bulletin of the American Meteorological Society*, *91*(8), 1015–1058.

Saha, S., Moorthi, S., Wu, X., Wang, J., Nadiga, S., Tripp, P., ... others (2014). The NCEP climate forecast system version 2. *Journal of climate*, *27*(6), 2185–2208.

Saini, J., Stein, R., Fahl, K., Weiser, J., Hebbeln, D., Hillaire-Marcel, C., & de Vernal, A. (2020). Holocene variability in sea ice and primary productivity in the northeastern Baffin Bay. *arktos*, *6*(1), 55–73.

Schauer, U., & Beszczynska-Möller, A. (2009). Problems with estimation and interpretation of oceanic heat transport–conceptual remarks for the case of Fram Strait in the Arctic Ocean. *Ocean Science*, *5*(4), 487–494.

Schauer, U., Fahrbach, E., Osterhus, S., & Rohardt, G. (2004). Arctic warming through the Fram Strait: Oceanic heat transport from 3 years of measurements. *Journal of Geophysical Research: Oceans*, *109*(C6).

Schulze Chretien, L. M., & Frajka-Williams, E. (2018). Wind-driven transport of fresh shelf water into the upper 30 m of the Labrador Sea. *Ocean Science*, *14*(5), 1247–1264.

Smith, B., Fricker, H. A., Gardner, A. S., Medley, B., Nilsson, J., Paolo, F. S., ... Zwally, H. J. (2020). Pervasive ice sheet mass loss reflects competing ocean and atmosphere processes. *Science*. doi: 10.1126/science.aaz5845

Smith, G. C., Allard, R., Babin, M., Bertino, L., Chevallier, M., Corlett, G., ... others (2019). Polar ocean observations: a critical gap in the observing system and its effect on environmental predictions from hours to a season. *Frontiers in Marine Science*, *6*, 429.

Smith, R., & Gent, P. (2002). Reference manual for the Parallel Ocean Program (POP). *Los Alamos unclassified report LA-UR-02-2484*.

Stewart, A. L., Klocker, A., & Menemenlis, D. (2018). Circum-Antarctic shoreward heat transport derived from an eddy-and tide-resolving simulation. *Geophysical Research Letters*, *45*(2), 834–845.

Stewart, A. L., & Thompson, A. F. (2015). Eddy-mediated transport of warm Circumpolar Deep Water across the Antarctic shelf break. *Geophysical Research Letters*, *42*(2), 432–440.

Straneo, F., & Heimbach, P. (2013). North Atlantic warming and the retreat of Greenland's outlet glaciers. *Nature*, *504*(7478), 36–43.

Straneo, F., Heimbach, P., Sergienko, O., Hamilton, G., Catania, G., Griffies, S., ... others (2013). Challenges to understanding the dynamic response of Greenland's marine terminating glaciers to oceanic and atmospheric forcing. *Bulletin of the American Meteorological Society*, *94*(8), 1131–1144.

Straneo, F., Sutherland, D. A., Holland, D., Gladish, C., Hamilton, G. S., Johnson, H. L., ... Koppes, M. (2012). Characteristics of ocean waters reaching Greenland's glaciers. *Annals of Glaciology*, *53*(60), 202–210.

Sutherland, D. A., & Pickart, R. S. (2008). The East Greenland coastal current: Structure, variability, and forcing. *Progress in Oceanography*, *78*(1), 58–77.

Sutherland, D. A., Straneo, F., Stenson, G. B., Davidson, F. J., Hammill, M. O., & Rosing-Asvid, A. (2013). Atlantic water variability on the SE Greenland continental shelf and its relationship to SST and bathymetry. *Journal of Geophysical Research: Oceans*, *118*(2), 847–855.

Trodahl, M., & Isachsen, P. E. (2018). Topographic influence on baroclinic instability and the mesoscale eddy field in the northern North Atlantic Ocean and the Nordic Seas. *Journal of Physical Oceanography*, *48*(11), 2593–2607.

Tsubouchi, T., Bacon, S., Naveira Garabato, A., Aksenov, Y., Laxon, S. W., Fahrbach, E., ... Ingvaldsen, R. (2012). The Arctic Ocean in summer: A quasi-synoptic inverse estimate of boundary fluxes and water mass transformation. *Journal of Geophysical Research: Oceans*, *117*(C1).

van den Broeke, M., Bamber, J., Ettema, J., Rignot, E., Schrama, E., van de Berg, W. J., ... Wouters, B. (2009). Partitioning recent Greenland mass loss. *Science*, *326*(5955), 984–986.

Wang, H., McClean, J. L., Talley, L. D., & Yeager, S. (2018). Seasonal cycle and annual reversal of the Somali Current in an eddy-resolving global ocean model. *Journal of Geophysical Research: Oceans*, *123*(9), 6562–6580.

Wouters, B., Chambers, D., & Schrama, E. J. O. (2008). GRACE observes small-scale mass loss in Greenland. *Geophysical Research Letters*, *35*(20). (L20501) doi: 10.1029/2008GL034816